2010

Laser Plasma Radiation Studies For Droplet Sources In The Extreme Ultraviolet

Reuvani Kamtaprasad
University of Central Florida

STARS Citation

Kamtaprasad, Reuvani, "Laser Plasma Radiation Studies For Droplet Sources In The Extreme Ultraviolet" (2010). *Electronic Theses and Dissertations, 2004-2019*. 4338.
https://stars.library.ucf.edu/etd/4338

Laser Plasma Radiation Studies for Droplet Sources in the Extreme Ultraviolet

by

Reuvani D. Kamtaprasad
B.S. University of Central Florida, 2007

A thesis submitted in partial fulfillment of the requirements
for the degree of Master of Science
in the School of Electrical Engineering and Computer Science
in the College of Engineering and Computer Science
at the University of Central Florida
Orlando, Florida

Spring Term
2010

Major Professor: Martin C. Richardson

ABSTRACT

The advancement of laboratory based Extreme Ultraviolet (EUV) radiation has escalated with the desire to use EUV as a source for semiconductor device printing. Laser plasmas based on a mass-limited target concept, developed within the Laser Plasma Laboratory demonstrate a much needed versatility for satisfying rigorous source requirements. This concept produces minimal debris concerns and allows for the attainment of high repetition rates as well as the accommodation of various laser and target configurations.

This work demonstrates the generation of EUV radiation by creating laser plasmas from mass-limited targets with indium, tin, and antimony doped droplets. Spectral emission from the laser plasmas is quantified using a flat-field spectrometer. COWAN code oscillator strength predications for each of the dopants were convolved with narrow Gaussian functions creating synthetic spectra for the EUV region between 10 nm - 20 nm. A preliminary comparison was made between the theoretical spectra and experimental results. From this comparison, ion stage transitions for each of the hot dense plasmas generated were assessed.

To my mother and father

ACKNOWLEDGMENTS

I would like to begin by expressing my humble gratitude to Professor Martin Richardson. Since I joined the LPL family as an IREU student, he has continued to support my efforts with encouragement and numerous research opportunities.

I would also like to thank Dr. Kazutoshi Takenoshita for providing me mentorship in my initial EUV experiments and Dr. Matthieu Baudelet for being my plasma physics guru.

Thank you Dr. Moza Al-Rabban for providing me with atomic physics calculations and providing so much insight in my Master's thesis.

Thank you to the members of my EUV Team: Omar Rodriguez, Nathan Bodnar and John Szilagyi. We have gone over hills and mountains in our experiments and I don't know how we would have ever survived them if we didn't work so well as a team. Thank you to the rest of the LPL family for always sharing intellectual conversations as well as amusing lab stories. I am delighted that I will be continuing my work as a PhD student with such an enthusiatic group.

Lastly, I would like to thank my parents and my sister, Hema. Thank you so much for being supportive and encouraging me to reach beyond the stars. I love you all so much and I hope to continue making you proud!

TABLE OF CONTENTS

LIST OF FIGURES

LIST OF TABLES

LIST OF ACRONYMS

ADT — Alpha Demo Tool
CCD — Charge Coupled Device
CE — Conversion Efficiency
CH_3OH — Methanol
CXRO — Center for X-Ray Optics
DPP — Discharge Produced Plasma
EUV — Extreme Ultraviolet
EUVL — Extreme Ultraviolet Lithography
FC — Flying Circus
FFS — Flat-Field Spectrometer
HHG — High Harmonic Generation
HVM — High Volume Manufacturing
IBA — Inverse Bremsstrahlung
IF — Intermediate Focus
In — Indium
$InCl_3$ — Indium Chloride
ITRS — International Technology Roadmap for Semiconductors
LPL — Laser Plasma Laboratory
LPP — Laser Produced Plasma
LTE — Local Thermal Equilibrium
MCP — Micro-Channel Plate
MFS — Minimum Feature Size
MLM — Multi-Layered Mirror
NA — Numerical Aperture
Nd:YAG — Neodymium-Doped Yttrium Aluminium Garnet
Sb — Antimony
$SbCl_3$ — Antimony Chloride
Sn — Tin
$SnCl_2$ — Tin Chloride
TIR — Total Internal Reflection
UTA — Unresolved Transition Array

CHAPTER 1
INTRODUCTION

History has shown that although plentiful in the sun's rays, the radiation region known as Extreme Ultraviolet (EUV) has been challenging for science and engineering to explore. This spectral region, defined from 30 eV (40 nm) to 250 eV (5 nm) as shown in Figure 1.1, lies between the ultraviolet and x-ray bands and is one of the last regions to be researched [1]. The main characteristic that distinguishes EUV from longer wavelengths is its short absorption length ($\approx 1\mu$m). EUV photon energies exceed the band gap of almost all material. In this range, photon energies reach sufficient values to photon-ionize many materials and photon-electron scattering becomes appreciable. Thus, conventional transmissive optics such as lenses and windows can not be used in the EUV. Most reflective optics are also untenable because many materials do not reflect EUV well at normal incidence and grazing angle optics are only operable at a few degrees. Given that air and many gases also absorb in the EUV, most experiments must be conducted under vacuum conditions [2].

Despite these limitations, exploration into EUV wavelengths provide mechanisms for both elemental (C, N, O, etc) and chemical (SiO_2, $TiSi_2$) speciation, creating new scientific progress [1]. These include, but are not limited to studies in astronomy such as EUV emission in the sun and various celestial matter, as well as technological advancement for fabrication in the semiconductor industry (attainment of smaller feature sizes on microchips) and microscopy (study of live cellular organisms).

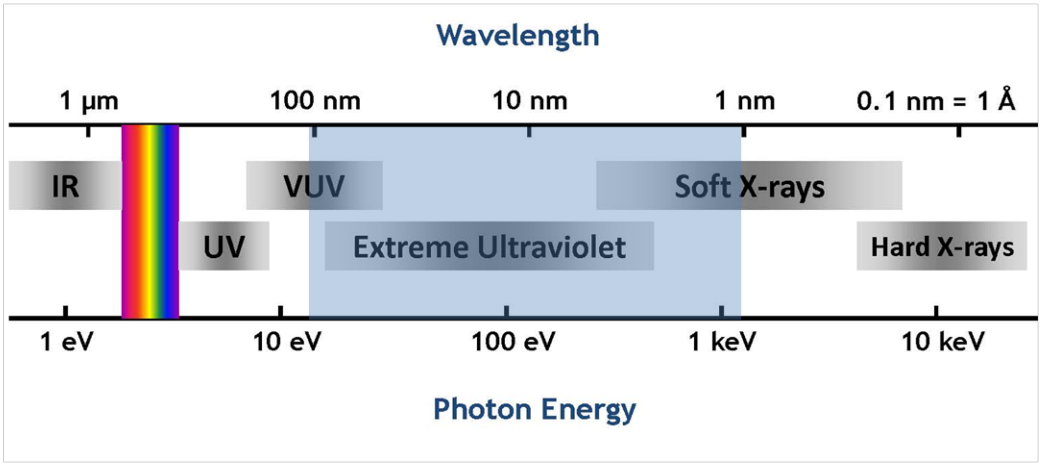

Figure 1.1: Electromagnetic Spectrum

1.1 Optics for EUV Light

Layered structures where the refractive index alters periodically with depth will reflect electromagnetic waves at specific wavelengths. This phenomenon is seen in natural crystals that demonstrate Bragg diffraction of x-rays. Soon after x-ray diffraction theory was developed, it was realized that if these mechanisms could be created artificially, they could function as Bragg diffractors and serve as valuable experimental instruments [3]. EUV's ability to absorb in many materials introduces a need for such structures. Multilayer mirrors (MLMs) are a new form of reflectors, enabled by the precision deposition and patterning technology of the microelectronic industry [4]. Their theory adapts the Bragg diffraction phenomenon and is based on constructive interference. MLMs consist of two materials, alternating high and low Z (atomic number) layers [5] . Each pair of layers functions such that incoming EUV radiation is scattered, or redirected without otherwise being altered. Scattering follows Bragg's corrected law of refraction given as [1]:

$$m\lambda = 2dsin\theta\sqrt{1 - \frac{4\bar{\delta}d^2}{m^2\lambda^2}} \tag{1.1}$$

where θ is the angle between the incident ray and the scattering ray, m is the diffraction order, d is the layer pair periodicity ($d = \lambda/2$) and δ is the bilayer weighted real part of the refractive index. This principle is illustrated in Figure 1.2.

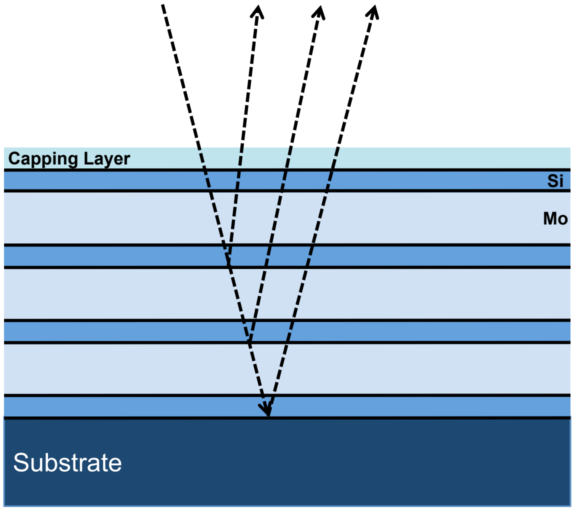

Figure 1.2: Bragg's Corrected Law of Refraction

The high Z material in the mirror is often thicker than its counterpart and is used to weaken absorption and provide scattering, while the low Z material is used as a spacer because its absorption coefficient is much lower. Multilayer coatings for reflective optics for EUV projection lithography systems are typically designed to consist of layers of molybdenum (Z = 42) and silicon (Z = 14) (Mo/Si) or molybdenum and beryllium (Z = 4) (Mo/Be). The theoretical peak reflectance of a Mo/Si MLM is 70%, however, this value is subdued because of diffusion at the layer interfaces. Currently, Mo/Si mirrors with peak reflectances of 67.5% at 13.4 nm can be routinely achieved [6, 7].

Figure 1.3 is a theoretical simulation of a molybdenum-silicon multilayer optic with a periodicity of 40, designed using the Center for X-Ray Optics (CXRO) website [8]. The wavelength of peak reflectivity can be adjusted by varying the layer spacing. The figure shows a peak at 13.5 nm and has properties similar to those used within the EUV community.

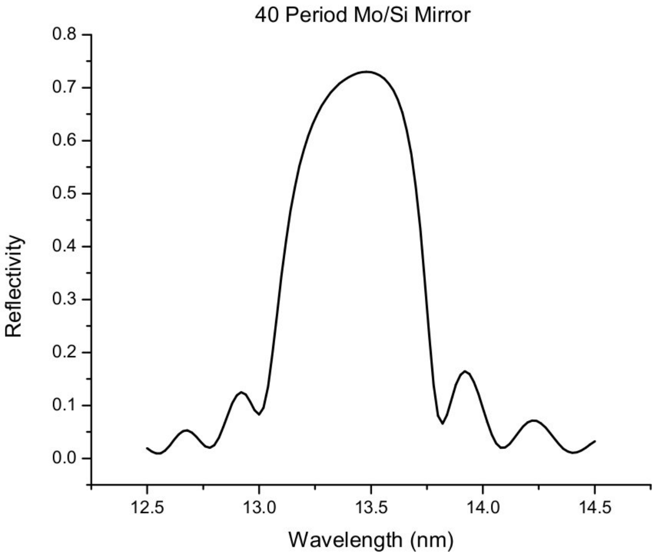

Figure 1.3: Simulated reflectivity of a 40 pair Mo-Si multilayer optic acquired from CXRO multilayer reflectivity design webpage
[8]

The introduction of carbon and silicon carbide diffusion barriers, in between the molybdenum and silicon layers has aided in the enhancement of reflectivity and the stabilization of MLM optics [9].

1.2 Applications of EUV Sources

Progress in fabricating multilayer optics has escalated scientific research in both laboratory and celestial extreme ultraviolet sources. Applications of laboratory EUV include high powered sources for nanoscale imaging and printing.

With the need to keep up with Moore's law and the International Technology Roadmap for Semiconductors (Figure 1.4), laboratory EUV source development has made one of its most significant contributions in the semiconductor industry.

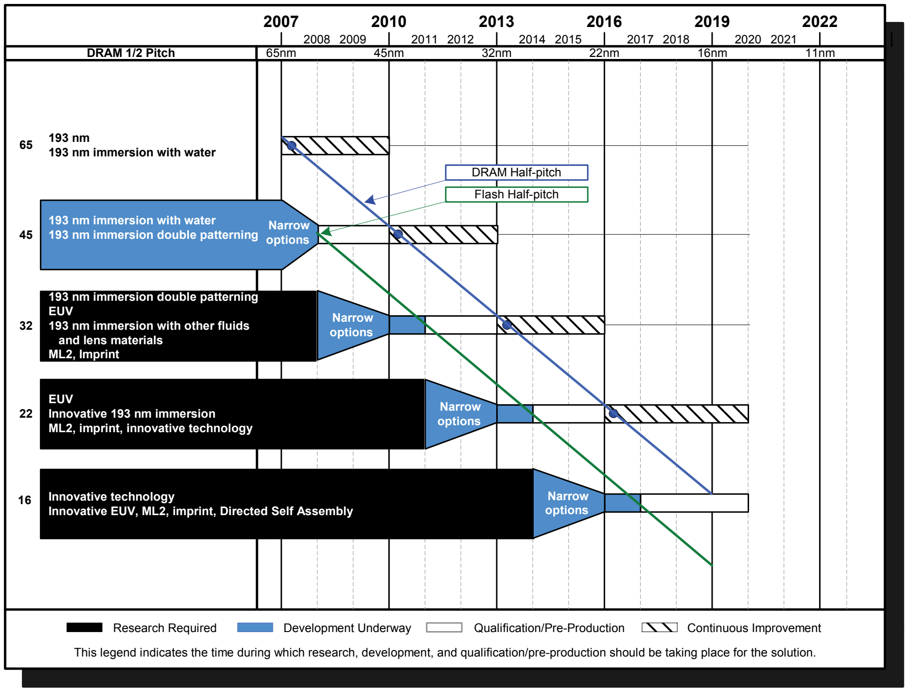

Figure 1.4: 2007 ITRS lithography roadmap for semiconductors [10]

Derived from Rayleigh's resolution formula, the minimum feature size (MFS) for circuit printing shown in Equation 1.2 is dependent on the process constant, k_1, the numerical aperture, NA, of the optical system and the exposure wavelength, λ [11].

$$\mathrm{MFS} = \frac{k_1 \lambda}{NA} \tag{1.2}$$

The use of an EUV source for lithography considerably decreases the exposure wavelength, hence reducing the minimum feature size on wafers from 193-248 nm to lower than 16 nm [12]. Figure 1.5 shows an illustration of multilayered optics being used in the stepper process for EUV lithography (EUVL). The promising results of EUVL does not come cheap. This latest step in the semiconductor industry also proves to be the most complicated, introducing challenges such as industry specified source requirements, new photoresist development and new masking techniques.

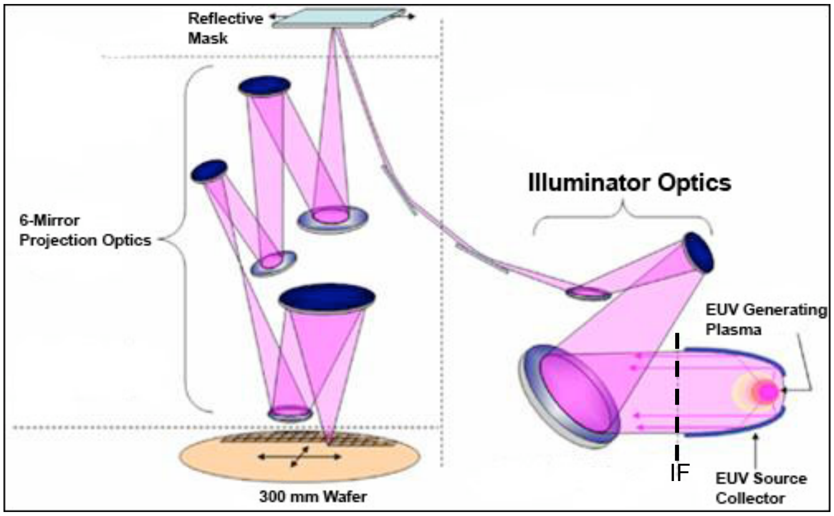

Figure 1.5: EUVL Stepper Process using multilayered optics

The physical requirements for an EUV source for use in Beta Stepper Tools as well as High Volume Manufacturing (HVM) are displayed in Table 1.1 [11]. Beta Tools are similar to HVM tools in that they have the same optics and require the same processing methods [11].

The 115 W power requirement has for many years, been the most critical factor, as judged by the combined representatives of the chip manufacturers. This is because the source output directly affects the wafer throughput and responsiveness of photoresist during exposure. Assuming a field size of 25 mm x 25 mm and 89 fields in a wafer with a resist sensitivity of 5.0 mJ/cm^2, the energy needed to expose all fields in the wafer is 2.9 J. However, prior to

Table 1.1: EUV Source Requirements

Requirement	**Beta 2009**	**HVM 2011**
Wavelength (nm)	13.5	13.5
Throughput (wafers/h)	60	100
EUV Power at IF (W)	30	115
Repetition Rate (kHz)	5	7-10 (no upper limit)
Energy Stability (%)	–	0.3
Collector Lifetime (h)	–	>30000
Etendue (mm^2)	–	<3.3
Max. Solid Angle to Illuminator (sr)	–	0.03-0.2

meeting the wafer, the power requirement of the source must first meet illumination, reticle and projection optics box conditions. Taking into consideration component degradation factors, it has been expected that 115 W of EUV light will be needed at intermediate focus (IF), the interface between the EUV source and illumination optics.

Source lifetime and stability are also challenges that have proved to be difficult to overcome. The estimated 3 year lifetime goal is influenced by several parameters, including degradation of the primary collector mirror. Stability of the stepper is directly related to the stability of the EUV source and the source stability is highly influenced by its repetition rate. Ideal repetition rates are estimated to be approximately 10 kHz [11, 13].

Present day management of these hurdles has allowed EUVL to remain the leading candidate for semiconductor manufacturing of technology nodes below the 22 nm range. ASML, the largest supplier of photolithographic systems in the world, recently demonstrated an EUV full-field scanner, the ADT (Alpha Demo Tool), used successfully for EUV development prior to the installation of their pre-production tool. The ADT uses a discharge produced plasma, 120 W tin target source producing an EUV output power of 5.3 W [14]. The system operates with a numerical aperture (NA) of 0.25 on a field size of 26 mm x 24 mm and was demonstrated for a 9 month period thus far. [15, 16].

The advancement of multilayer optics has also played a significant role in astronomical studies. Optical systems, such as Cassegrain telescopes, are used to capture high resolution images with the aid of Mo-Si multilayered optics [17]. Other applications include High-Harmonic-Generation based EUV lasers (which are discussed briefly in Chapter 2) and EUV microscopy. EUV microscopy ranges from biological imaging to specialized imaging for lithographic purposes such as defect inspection of EUV masks that support the advancement of EUVL [18].

CHAPTER 2
EUV SOURCE CONCEPT

Techniques for producing laboratory EUV radiation include continuous sources such as e-beam devices, pulsed sources (developed from discharge and laser produced plasmas) and coherent sources based on high harmonic generation lasers or e-beam soft x-ray lasers. The emphasis of this study is the laser produced plasma source. The advantages and disadvantages of this source and several others are discussed in this chapter.

2.1 Synchrotron Sources

Large cyclic electron accelerators called synchrotrons are the most dependable and important sources for EUV and soft x-ray emission. These particle accelerators rely on strong magnetics fields that allow electrons to travel at relativistic speeds in a curved trajectory resulting in radiation emission [19]. First generation synchrotron geometries were simple circular rings under ultra high vacuum pressures (10^{-9} Torr). Many current synchrotrons (second generation) involve storage rings of more complex, quasi-polygonal designs. Newer synchrotron facilities (third generation) have many straight sections that are separated by a series of 'bending' magnets (Figure 2.1). As the electrons circulate the storage rings, they are diverted by magnetic fields, emitting electromagnetic radiation at each bending magnet. These beams are then captured and focused to specific wavelengths [20].

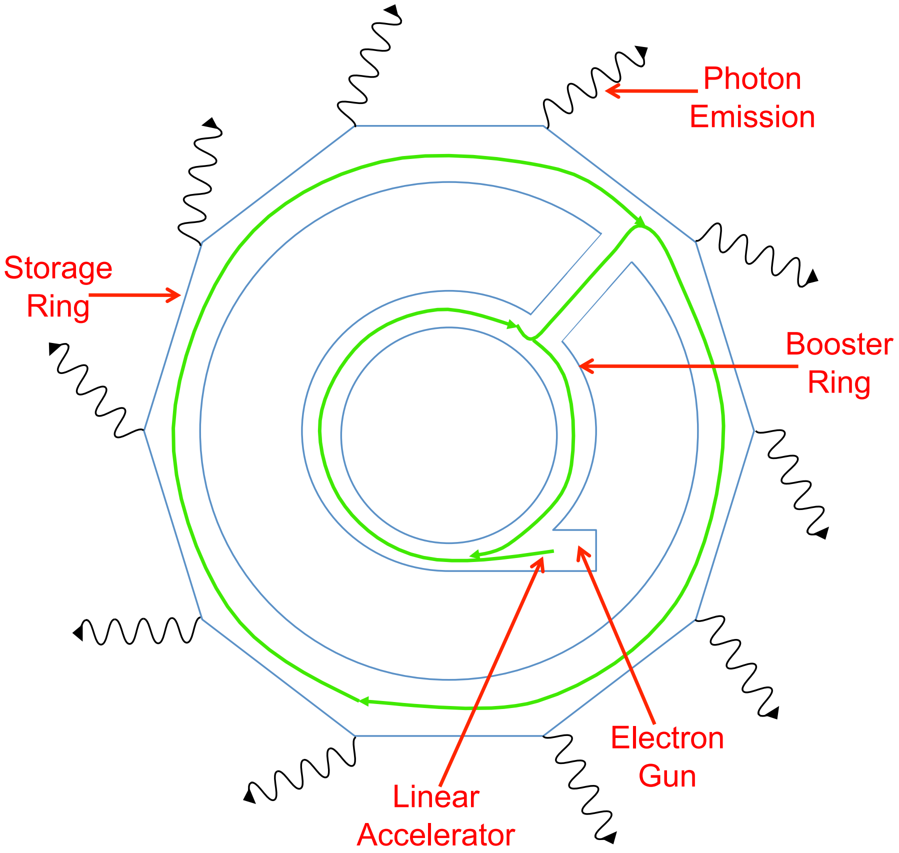

Figure 2.1: Synchrotron Radiation Facility

Third generation facilities also use insertion devices in the booster ring to significantly increase the intensity of the emitted radiation as seen in Figure 2.2. These are called wigglers and undulators. Wigglers have large magnetic fields with strong harmonics extending into higher photon energies. They operate such that at each bend in the wiggle, a conical beam is produced. Each of these is re-collimated with optics to form beam lines. Beam lines are normally associated with different wavelength and optical properties [21].

Undulators use weaker magnetic fields but produce greater intensities of light than wigglers. The magnets are arranged such that the light cones overlap and interfere with one another at specified wavelengths. The radiation of choice can be tuned by changing the gap between the magnets. Undulator radiation provides high spectral brightness, partial coherence, tunability and narrow bandwidth [22].

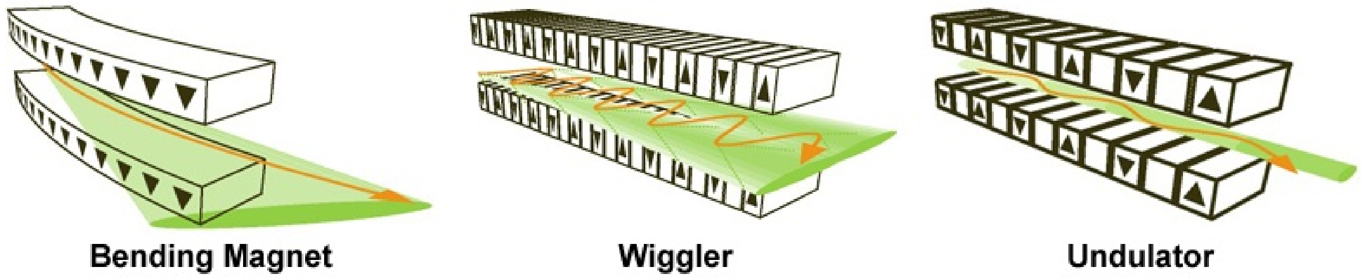

Figure 2.2: Radiation techniques at advanced synchrotron facilities (Courtesy of the Austrailian Synchrotron Facility)
[22]

Synchrotron radiation is a desirable source for short wavelength emission, however facilities are large and expensive with a limited number of locations around the world. Therefore this source is not practical for applications such as microscopy and EUVL. A less costly, more compact source is sought after.

2.2 Discharge Sources

Discharge produced plasmas (DPP) have become a popular candidate for EUV emission. These plasmas are created when a large potential difference is sent across a column of gas, forcing an electrical breakdown in the gas [20]. The configuration for a discharge produced plasma source is shown in Figure 2.3. Principal light collectors are nested cylindrical, ellipsoidal or Wolter-type grazing incidence mirrors. Systematic DPP source development for chip manufacturing began with Xenon targets using various concepts, all involving several types of pinch plasmas.

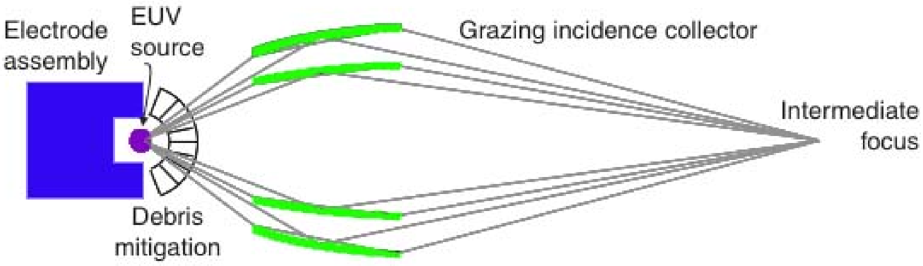

Figure 2.3: Configuration of a discharge produced plasma [11]

To produce an intense plasma state, the DPP must be heated and experience a so-called "pinch effect" in which a transient linear current goes through the plasma inducing a magnetic force that confines and compresses the plasma [11, 23]. The design of discharge plasmas are simple and compact and offer a variety of different electrode geometry configurations making it a convenient source for many applications. The conversion efficiency (CE) for this source scheme is simply the ratio of input electrical power to the power of the plasma source output. Tin based DPPs have reached CEs of 2.5% [11].

A variety of discharge schemes have been investigated as sources for EUV lithography. However, the challenges faced with incorporating DPP sources into EUV steppers are largely technical. Resolving these matters will include continued study on the maintenance of high repetition rates for stability and thermal management mechanisms. DPPs also suffer from debris as a result of electrode erosion. This drawback is a common challenge among all plasma sources and leads to damage of collector optics and significant degradation of source lifetimes [24]. A long source lifetime is a requirement for lithography so debris mitigation is an important issue that must be addressed. One of the most popular debris mitigation mechanisms for DPP sources is the so-called 'foil trap' (shown in Figure 2.4). A foil trap is a nested set of closely spaced vanes that reduces sputter of optical surfaces. Debris particles are captured onto the foil linings which are positioned in radial directions with respect to the source location [25, 26].

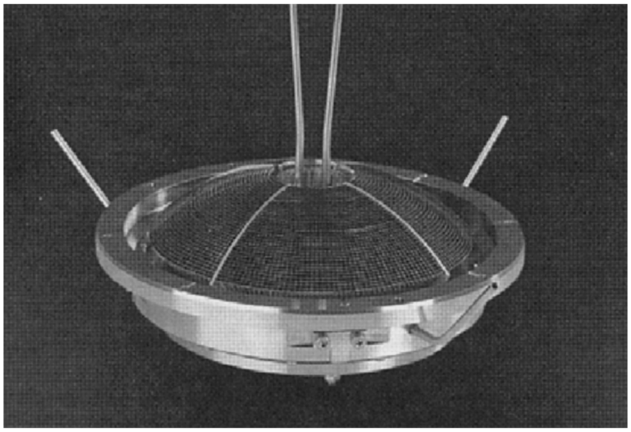

Figure 2.4: Foil trap filter for debris mitigation
[25]

2.3 EUV Lasers and Femtosecond High Harmonic EUV

EUV Lasers and High Harmonic Generation (HHG) allow for the creation of spatially coherent sources of EUV and Soft X-Ray light. EUV lasers use discharge or laser produced plasmas as active media to create high energy wavelength light amplification. A simplification of the capillary discharge plasma operation for coherent EUV is shown in Figure 2.5. Phase matching of the conversion process is what creates coherent EUV. Although not nearly as high powered or mature as lasers in the visible or infrared, table-top EUV lasers have sparked plenty of interest in both the laser development and semiconductor industries with applications such as nanoscale imaging and ablation as well as table top EUV interferometry. Currently, EUV lasers have powers of 1-5 μW with sub-femtosecond pulse durations and laser observed wavelengths as short as 10.9 nm [27].

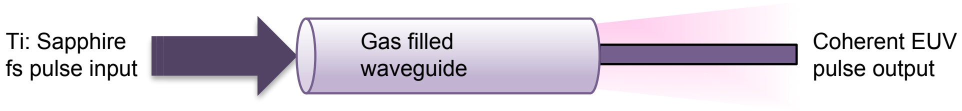

Figure 2.5: Femtosecond laser is focused into a gas filled waveguide to produce coherent EUV output

2.4 Laser Plasma Source

Like DPPs, Laser Produced Plasma (LPP) EUV sources must accommodate very high performance requirements to qualify as a conceivable technology in the microchip fabrication industry. These sources are created by optical laser-target coupling and therefore one of the benefits of LPPs is that the laser and associated apparatus do not need to be physically located near the plasma source or scanner equipment. This is unlike DPPs which require power systems and cooling mechanisms to be integrated near or at the source location. LPPs also allow for higher repetition rates (up to several tens of kilohertz), generating higher doses of stability [28].

Laser plasmas are created by ionizing a target surface as a direct result of focusing a sufficiently high intensity laser beam onto it. The common configuration for an LPP light source is shown in Figure 2.6.

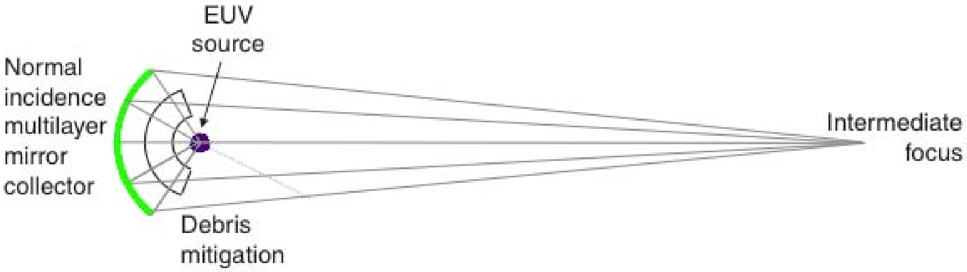

Figure 2.6: Configuration of a laser produced plasma
[11]

The hot dense plasma produces both continuum and discrete radiation as a result of the target material. Its ”fingerprint” is identified by characteristics such as temperature and density. These traits are determined by target architecture, chemical composition and by the laser’s attributes. Laser irradiance is defined as:

$$I = \frac{E}{A\tau}\left(\frac{W}{cm^2}\right) \tag{2.1}$$

where E is the beam energy in joules, A is the area of the focused spot size of the beam in cm^2 and τ is its pulse duration in seconds. The intensity plays a key role in generating optimum plasma characteristics.

Considering the flexibility of laser plasmas, they arguably offer less severe complications as an integrated lithographic source, particularly bearing in mind the thermal dissipation matters associated with discharge plasmas [28]. Debris mitigation still becomes a problem when choosing a viable EUV plasma source. This consequence was recognized by the Laser Plasma Laboratory from the outset of our involvement in sources for EUVL. A unique method for creating mass-limited droplet targets was devised. Target configuration for mass-limited droplets minimizes large debris issues obtained when generating laser plasmas from planar targets. This documentation is concerned with developing and examining these mass-limited targets for various material compositions and will be examined thoroughly in subsequent chapters.

CHAPTER 3
PHYSICAL PROCESSES IN LASER PLASMAS

Plasmas are considered by many to be the fourth state of matter because they possess properties unlike those of solids, liquids and gases. Since this thesis presents the development of hot dense plasmas, this chapter concerns itself with presenting the physics behind these plasmas. The chapter begins by discussing general plasma conditions and then continues to describe characteristics of laser plasmas, examining both blackbody radiation (considering equilibrium effects) and spectral emission as a diagnostic for understanding non-equilibrium effects. These phenomenons are examined more thoroughly in many texts including [11, 28, 29, 31, 33, 38, 39]

3.0.1 Basic Plasma Physics

To understand the nature of laser plasmas, it is important to understand the physical processes behind all plasmas. A plasma is defined as a system of ions and electrons, having a total neutral charge, which are coupled to each other via their self-consistent electric and magnetic fields [29]. When not in equilibrium, displaced ions and electrons pull towards each other from the resulting electric field allowing both electrons and ions to oscillate. However, because the ions have a much larger mass than their electron counterparts, they are assumed to be stationary and the electron oscillations overpower the ions.

The frequency of this electron oscillatory effect is called the electron plasma frequency, ω_p, and is defined as:

$$\omega_p = \sqrt{\frac{n_e e^2}{\epsilon_0 m_e}} \tag{3.1}$$

where n_e is the electron density, e is the charge of an electron (1.6022 x 10^{-19} C), ϵ_0 is the permittivity of vacuum (8.854 x 10^{-12} F/m) and m_e is the mass of an electron (9.1094 x 10^{-31} kg). The nature of oscillating waves within the plasma causes these particles to interact with the electromagnetic fields which creates a dispersion effect as described by

$$w_0^2 = w_p^2 + c^2k^2 \tag{3.2}$$

where ω_0 is the angular frequency of the incident light, c is the speed of light ($\approx$ 3 x 10^8 m/s) and k is the wave number ($2\pi/\lambda$). From these two equations, the index of refraction can be derived [30] to be

$$n(n_e, \omega_0) = \frac{ck}{\omega_0} = \sqrt{1 - \frac{w_p^2}{w_0^2}} = \sqrt{1 - \frac{n_e e^2}{\epsilon_0 m_e \omega_o^2}} \tag{3.3}$$

When light travels to high electron densities, it should be noted that ω_p will approach ω_0 and the index of refraction will approach zero. This results in total internal reflection (TIR) and also the derivation of the critical density defined as:

$$n_{cr} = \frac{\epsilon_0 m_e \omega_0^2}{e^2} \tag{3.4}$$

The critical density is where the index of refraction of a particular optical frequency goes to zero [30]. For the conditions required here, the laser light does not quite reach the critical density. The light is progressively absorbed on the sloping density front leading up to the critical density. This mechanism is known as Inverse Bremsstrahlung Absorption(IBA). IBA and several other processes such as resonance absorption and Raman scattering take place around the critical density region. EUV and Soft X-Ray emission also normally occurs around the critical density region where the highest thermal conduction is experienced. The critical density for an Nd:YAG laser, as was used for the experiments in this thesis, is $\approx 10^{21}\text{cm}^{-3}$.

3.0.2 Laser Plasma Physics

Basic concepts of all plasmas were discussed in the previous section. Laser plasmas, to be more specific, are produced when high intensity laser beams, which generate large electromagnetic fields, are focused onto a target surface to generate ionization. Laser radiation of intensities greater than $10^8\ W/cm^2$ provide large enough electric fields to breakdown target material. When the focused laser beam hits the target, multi-photon ionization is often initiated. A hot plasma conversion layer known as a corona is formed on the surface of the target. The initial ionization processes occurs much faster than the actual pulse duration of the laser beam so following pulses couple to the corona [11, 28, 31, 32]. This interaction leads to electron avalanche, a phenomenon where electrons endure high accelerations allowing them to collide with ions in the plasma and form new electrons that experience the same procedure, hence increasing the electron density of the plasma. The plasma expands normal to the surface of the target and the laser radiation energy continues to get absorbed. TIR is experienced when ω_p equals ω_L (formerly known as ω_0) and the laser beam is incident upon target. Reflected light is unacceptable and is prevented by controlling the slope of the laser. This is done by using long nanosecond pulsed lasers for plasma generation [33].

3.0.3 Inverse Bremsstrahlung

The most efficient absorption mechanism in laser plasmas is IBA which is also referred to as collisional absorption. Bremsstrahlung occurs when light is emitted by electrons slowing down in the vicinity of an ion. Inverse Bremsstrahlung occurs when the electron accelerates instead. It then avalanches creating additional collisions of oscillating electrons and ions after the electrons have gained energy from the laser pulse. These collisions result in disorder which allows for increased electron energy and play a central role in heating the plasma. The efficiency of IBA is related to the intensity of the laser radiation. High intensities lead to saturation of collisional absorption. The IBA absorption coefficient [31] is

$$k_{IB} = 3.10 \times 10^{-7} \cdot ln\Lambda \cdot \frac{Zn_e^2}{T_e^{\frac{3}{2}}} \cdot \frac{1}{\omega_L^2 \sqrt{1 - \left(\frac{\omega_p}{\omega_L}\right)^2}} \tag{3.5}$$

In the equation, $ln\Lambda$ is the Coulomb logarithm which is related to the minimum and maximum impact parameters (defined as shown in Equation 3.6 [34]), Z is the average charge per ion and T_e is the electron temperature.

$$ln\Lambda = ln\left[\frac{3k_B T_e 4\pi\epsilon_0}{Z^* e^2}\sqrt{\frac{k_B T_e \epsilon_0}{e^2 n_e}}\right] \tag{3.6}$$

The IBA coefficient shows that collisional absorption is strongest for high electron densities and low temperatures. The fraction of absorbed laser energy [35] after traversing a distance L is given as

$$\alpha_{abs} = 1 - exp(-k_{ib} \cdot L) \tag{3.7}$$

L is the laser plasma scale length and is a function of the expansion velocity of the plasma and the laser pulse duration [29]. To determine if a laser plasma is dominated by IBA, a specific intensity where IBA is greatly diminished has been identified [36]. This intensity is defined as

$$I^* = 10^{12} \cdot \frac{Z L_\mu f}{\lambda^4} \tag{3.8}$$

where L_μ is the plasma scale length in μm, Z is again the ion charge state, f is the flux limit and λ is the laser wavelength in μm. When $\mathrm{I} \ll \mathrm{I}^*$, IBA is prevalent and the plasma remains collisional. However, when $\mathrm{I} \gg \mathrm{I}^*$, the plasma is less collisional and IBA is weakened.

3.0.4 Thermal Process in Plasmas

Hot dense plasmas have a tendency to push up the threshold of non-linear processes experienced by plasmas in general. To create EUV and Soft X-Ray emission, particles existing in the plasma must have very high energies ($\gg$ 100 eV). Conservation of energy is then maintained because particle-particle interactions radiate high energies. This phenomenon is best explained with the consideration of blackbody radiation. The peak photon energy is related to the temperature of the radiative bodies therefore EUV and Soft X-Ray emissions

(30- 250 eVs) require very hot radiators. Also, the emission must come from a large number of particles compressed into a small volume, approaching densities similar to those of solids. This is how the term ”hot dense plasmas” came to be [29]. These conditions are far from equilibrium and hence the plasmas endure very short lifetimes. The high temperatures and therefore high particle velocities cause the plasmas to expand and cool rapidly. The electron temperatures in these plasmas range from a few eVs to hundreds of eVs and differ for different plasma geometries (ie. spherical, planar) [11].

For most laboratory plasmas, it is reasonable to assume that there exists a state of local thermal equilibrium (LTE). This suggests that although the plasmas are not temporally or spatially uniform, at a local region at any given time, equilibrium exists. At LTE, ion and electron temperatures are the same. This is due to the high frequency of electron and ion collisions which allows for sufficiently high energy transfer rates from electron to ions and vice versa [24].

Plasmas created from nanosecond laser pulses for high Z elements can not generally be considered to be in LTE. Considerable energy is converted into radiation (line and blackbody emission) which strongly affects the population of available energy states. This non LTE regime introduces more physical complications including photoelectric and recombination process and radiative de-excitation [34].

A plasma is also characterized by its optical thickness [37]

$$\tau(\omega) = \int k(\omega)dx \tag{3.9}$$

where $k(\omega)$ is the absorption coefficient per cm and x is the coordinate along the line of sight. Intensity relations corresponding to the blackbody curve signify a plasma which is optically thick ($\tau \gg 1$) and in equilibrium. If a plasma is optically thin ($\tau \ll 1$), the intensity is proportional to the plasma thickness and Planck's Blackbody Radiation Law will not hold. Instead, optically thin plasmas are examined through free-free, free-bound and bound-bound emission mechanisms which will be discussed later on in the text. Thermal equilibrium is rarely achieved in the hot dense short-lived plasmas that are created within the laboratory and therefore the mechanisms mentioned above will be examined later in this chapter.

3.1 Identifying Plasma Emission Characteristics

As mentioned before, equilibrium requirements are rarely met within laser plasmas. When the plasma gains thermal energy, the electronic transitions can be divided into three groups based on the discreteness of the energy spectrum of the initial and final states of the system. The processes which are bound-bound, free-free and free-bound emission will be discussed in this section, but again, much more information can be found in the sources mentioned at the beginning of Chapter 3.

3.1.1 Bound-Bound Transitions (Line Emission)

The bound-bound transition correlates to electronic transitions within a particle that occur from one discrete energy level to another. By virtue of the discrete energy levels, the electronic transitions result in either emission or absorption of the line spectra [38]. An emission line is formed when an electron makes a transition from one discrete energy level to a lower level, releasing a photon of a particular wavelength. Absorption is thus, the opposite process where an electron transitions to a higher energy level and absorbs a photon. The absorbed photons are represented as a drop in continuum spectra at the wavelength associated with the absorption. Line emissions stem from either resonance transitions or transitions between excited states with resonance having stronger effects. The spectral line emission rate [34, 39] is

$$P_{\zeta m' \to \zeta m} = N_{im'} \hbar \omega_{\zeta m' \to \zeta m} A(\zeta m' \to \zeta m) \tag{3.10}$$

where $N_{im'} A(\zeta m' \to \zeta m)$ is the number of transitions from the upper to the lower state per second per cm^3 and $\hbar \omega_{\zeta m' \to \zeta m}$ is the energy of the emitted photon and the transition energy ($E_{\zeta m'}$ - $E_{\zeta m}$). The line shape of the spectra can be influenced by several parameters including the natural lifetime for the transition from one state to another, the motion of the emission and the interaction of the particle with other particles and fields within the plasma. The spectral line emission is the most important radiation process in hot plasmas, especially high Z plasmas where the ions are not fully ionized. The simple line structure for emission line transitions is more useful for low Z plasmas. As the number of bound electrons is increased (as is the case for high Z plasmas), the bound-bound spectrum becomes more complicated and emission lines pack closer together. The lines become so tightly spaced that often their spacing is smaller than their own line width. As a group, they inherit the title unresolved transition array (UTA) [28, 39]. Assigning characteristic wavelengths to lines within this region is difficult because there are too many lines to identify single transitions [35]. Figure 3.1 shows the UTA of a solid tin target plasma in the EUV region.

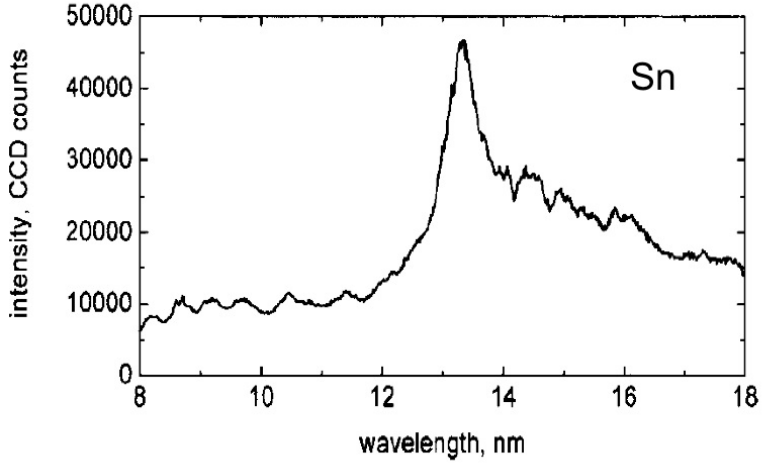

Figure 3.1: UTA in the EUV region for a solid tin target [35]

3.1.2 Free-Free Transitions (Bremsstrahlung Radiation)

Free-free transitions, also known as Bremsstrahlung radiation, occurs when a free electron moves through the electric field of an ion within a plasma cloud. The electron can emit a photon, losing all of its kinetic energy but remaining free, or it can gain a photon and gain even more kinetic energy [38]. The term Bremsstrahlung comes from the German words "bremse" meaning brake and "strahlung" meaning radiation. This term describes the free-free transition because the transition is made after the electron is deflected within the field of the ion and begins to slow down, losing some of its kinetic energy to radiation. Bremsstrahlung transitions result in continuum emission and absorption spectrums and depend on the electron density, electron temperature and ionic charge. The spectral energy density in terms of energy per volume per wavelength for Bremsstrahlung radiation [31] is

$$W_\lambda = 2 \times 10^{-27} \cdot \frac{Zn_e^2}{(T_e)^{0.5}} \cdot \frac{1}{\lambda^2} \cdot exp(-\frac{hc}{\lambda \cdot k_B T_e}) \tag{3.11}$$

Figure 3.2 is an animation of the bremsstrahlung radiation process. This process is useful for low Z target plasmas where the ions are fully ionized and little line emission is found. This is also true for higher Z plasmas where the ions are fully stripped. For high Z plasmas at low temperatures, the main mechanisms are line emission and bremsstrahlung radiation which provide low continuous background radiation [39].

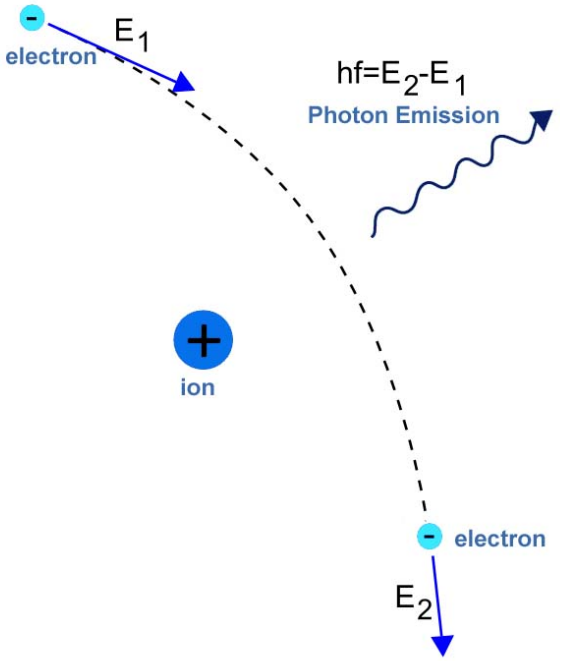

Figure 3.2: Bremsstrahlung radiation resulting in photon emisison

3.1.3 Free-Bound Transitions (Recombination Radiation)

Another means of continuum spectra are free-bound transitions or recombination radiation. This radiation process can only occur above the sharp, so-called ”edges” that refer to the binding energies of the bound state of the ions [39]. A free-bound transition can result from absorption of a photon. The electron will gain energy, exceeding that of its binding energy to the ion, and become free. The additional photon energy becomes kinetic energy of the free electron. The reverse can happen as well. The free electrons can be captured by the ions within the plasma and photons will be emitted. The spectral intensity of recombination radiation can be represented with respect to Bremsstrahlung radiation [31]

$$\frac{W_r}{W_B} \approx 2.4 \cdot \frac{Z^2 E_H}{k_B T_e} \tag{3.12}$$

In this ratio, E_H= 13.6 eV, the hydrogen ionization energy. The ratio depicts that Bremsstrahlung transitions overpower recombination in low Z and/or high temperature plasmas.

3.2 Plasma Simulation and Modeling

Characteristics of laser plasma emission is dependent on both laser and target parameters. To optimize the state of plasma emission, it is helpful to simulate plasma conditions and spectral expectations. The following section discusses three of these simulation programs used widely in the Laser Plasma Laboratory. MEDUSA and Vorpal are used to simulate various plasma attributes such as electron density and electron temperature. The COWAN code is implemented as a means of calculating atomic structures and spectra of various target elements.

3.2.1 Hydrodynamic Plasma Fluid Model

Prior to generating hot-dense plasmas for EUV radiation, the one-dimensional Lagrangian hydrodynamic code, MED 103, can be used to simulate hydrodynamic expansion of laser plasmas [35, 34, 40]. MED 103 is a popular and flexible plasma modeling code that was developed from an original MEDUSA code by Christiansen et. al. [41]. The code allows for the optimization of plasma conditions by allowing the user to modify parameters such as laser pulse duration, wavelength, laser intensity, target composition and atomic mass. The code outputs one-dimensional, 90-cell Lagrangian models that feature information on laser plasma coupling and expansion mechanisms and electron and radiation transport. Each cell contains specific information on the plasmas condition with respect to the lifetime of the plasma. Cell content includes electron and ion densities, plasma temperature, average ion state and other physical parameters of the plasma.

MED 103 was not used for optimizing the plasmas generated for this thesis. Input for the code requires an average atomic number for mixed layer targets such as the doped droplets used for these experiments. Tin doped plasmas, identical to those reproduced in this thesis were modeled in the PhD thesis of Dr. Chiew-Seng Koay [35]. His results are shown below. The adjacency of the elements used for this thesis (indium, tin and antimony) will lead to very similar plasma predictions for indium and antimony doped droplets.

One of the primary benefits of examining the plasma condition with MED 103 is the ability to determine the laser intensity input for optimum EUV emission. Koay used MED

103 for the characterization of a tin-doped water target and observed electron temperature and density as a function of laser intensities ranging from 1 x 10^{10} - 3 x 10^{13} W/cm^2. Figure 3.3 is a sample from Koay's work of input parameters used for this analysis.

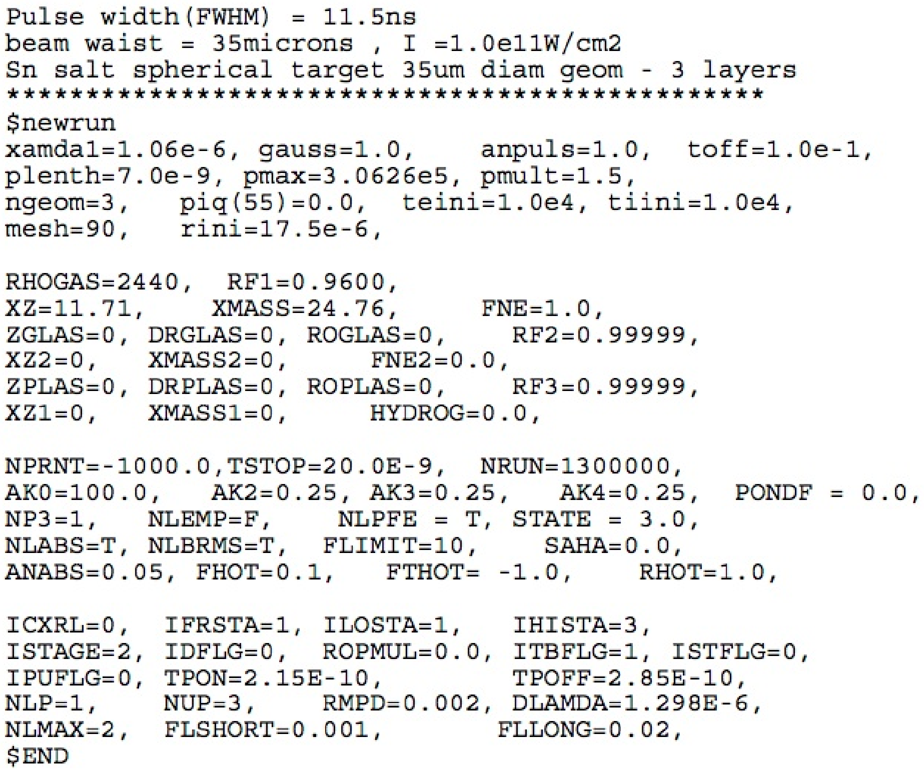

```
Pulse width(FWHM) = 11.5ns
beam waist = 35microns , I =1.0e11W/cm2
Sn salt spherical target 35um diam geom - 3 layers
************************************************
$newrun
xamda1=1.06e-6, gauss=1.0,    anpuls=1.0,  toff=1.0e-1,
plenth=7.0e-9, pmax=3.0626e5, pmult=1.5,
ngeom=3,   piq(55)=0.0,  teini=1.0e4, tiini=1.0e4,
mesh=90,   rini=17.5e-6,

RHOGAS=2440,  RF1=0.9600,
XZ=11.71,    XMASS=24.76,     FNE=1.0,
ZGLAS=0, DRGLAS=0, ROGLAS=0,    RF2=0.99999,
XZ2=0,   XMASS2=0,     FNE2=0.0,
ZPLAS=0, DRPLAS=0, ROPLAS=0,    RF3=0.99999,
XZ1=0,   XMASS1=0,     HYDROG=0.0,

NPRNT=-1000.0,TSTOP=20.0E-9,  NRUN=1300000,
AK0=100.0,   AK2=0.25, AK3=0.25,   AK4=0.25,  PONDF = 0.0,
NP3=1,   NLEMP=F,    NLPFE = T, STATE = 3.0,
NLABS=T, NLBRMS=T, FLIMIT=10,    SAHA=0.0,
ANABS=0.05, FHOT=0.1,   FTHOT= -1.0,    RHOT=1.0,

ICXRL=0,  IFRSTA=1, ILOSTA=1,   IHISTA=3,
ISTAGE=2, IDFLG=0,  ROPMUL=0.0, ITBFLG=1, ISTFLG=0,
IPUFLG=0, TPON=2.15E-10,        TPOFF=2.85E-10,
NLP=1,    NUP=3,    RMPD=0.002, DLAMDA=1.298E-6,
NLMAX=2,  FLSHORT=0.001,       FLLONG=0.02,
$END
```

Figure 3.3: Input parameters for MED 103 simulations
[35]

Figure 3.4 shows electron temperature and density results reported by Koay. R(μm) is the distance measured from the target center. It can be observed that the critical density point ($10^{21} cm^{-3}$), where IBA takes place, and the maximum electron temperature are located around the same region.

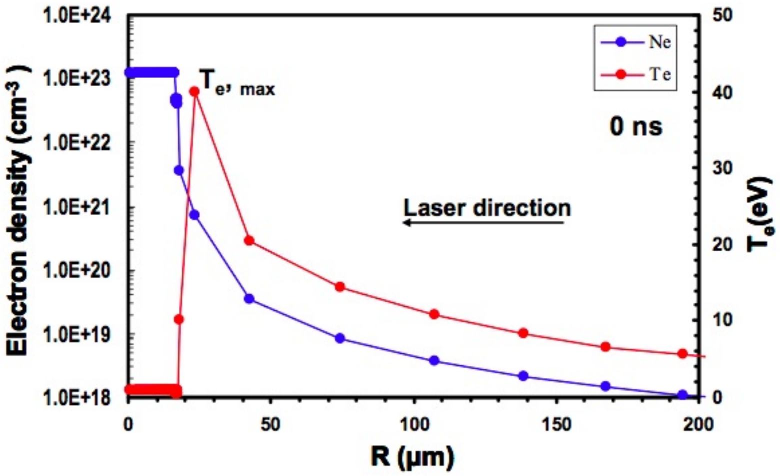

Figure 3.4: Electron temperature and density results at peak of laser input [35]

With these results Koay was able to identify that optimum EUV emission occurs with electron temperatures between 30 eV and 45 eV as was portrayed by previous models. Figure 3.5 is a plot of the maximum electron temperature as a function of laser intensity.

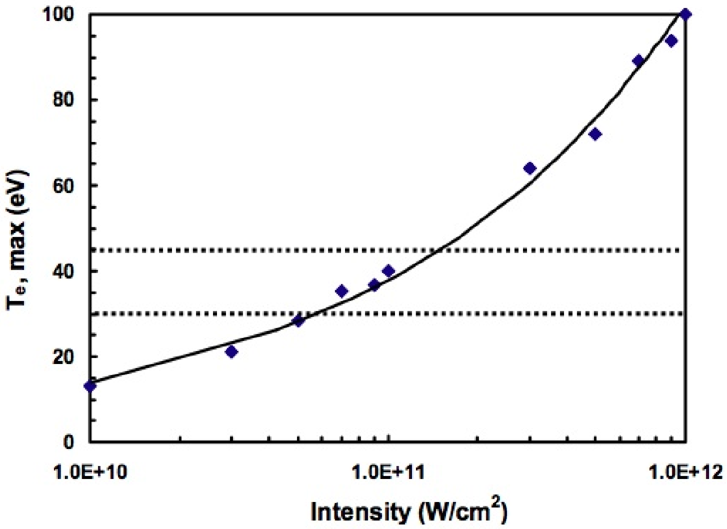

Figure 3.5: Electron temperature and density results at peak of laser input [35]

To optimize EUV emission conditions from a tin-doped target, laser intensity would be approximately 1 x 10^{11} W/cm^2. This is also the case for EUV emission from antimony and indium doped targets.

Vorpal is a GUI-driven hybrid plasma and beam simulation code. The software allows for textual or CAD input of more complicated geometrical target information. Vorpal simulations are governed using a three-dimensional cartesian grid. Positions relative to the grid are determined by particle-particle interactions and particle-field interactions [42]. Future work on the EUV plasmas generated for this thesis include a detailed analysis of plasma behavior and optimization of EUV emission using Vorpal.

3.2.2 Atomic Structure and Spectra

Plasma spectroscopy is the study of spectral characteristics of emitted radiation that allows for the understanding of the state of plasmas. Transition probabilities or oscillator strengths are a means of predicting spectral emission prior to experimentation. Transition probabilities for indium, tin and antimony ions have been deduced using the COWAN code suites [43] by Dr. Moza Al-Rabban of Qatar University. These calculations are presented in Chapter 5 of this thesis along with experimental results of the respective dopant material. In this section, the theoretical development leading to the transition strength predictions is presented as was described by R. D Cowan in [43].

For an isolated, field-free atom with a total angular momentum J_i, there are g_i degenerate quantum states for the Energy E_i where g_i is defined as:

$$g_i = 2J_i + 1 \tag{3.13}$$

The value $2J_i + 1$ corresponds to the number of possible values for M_i, the magnetic quantum number. A_{ji} or the Einstein A-coefficient describes the spontaneous transition probability per unit time of an electron in a specific excited state, j, making a transition to any of the g_i states of lower energy. This function is given as [20, 43, 44]

$$A_{ji} = \sum_{M_i} a_{ji} \tag{3.14}$$

It is more desirable to define a term for the weighted transition probability then the Einstein transition probability because it is more symmetric with respect to upper and lower energy levels. The weighted transition is defined as

$$g_j A_{ji} = \sum_{M_j} \sum_{M_i} a_{ji} \tag{3.15}$$

Assuming isotropic excitation and the same number of atoms in each state is of level j, the intensity of a line emission is calculated to be

$$I(t) = hc\sigma_{ji} g_i A_{ji} N_j(t) \tag{3.16}$$

In this equation, N_j(t) is the number of atoms in the state j and σ_{ji} is the spectrum line or wave number which is defined as

$$\sigma_{ji} = \frac{1}{\lambda_{ji}} = \frac{E_j - E_i}{hc} \tag{3.17}$$

The spontaneous transition probability can also be represented as a function of Einstein's absorption coefficient, B_{ij} and stimulated emission coefficient, B_{ji}.

$$g_j A_{ji} = 8\pi hc\sigma_{ji}^3 g_j B_{ji} \tag{3.18}$$

where

$$g_j B_{ji} = g_i B_{ij} \tag{3.19}$$

From Equation 3.18, it is clear to see that g_j is seen to always represent the statistical weight of the initial level therefore $g_j A_{ji}$ can simply be represented as gA. The intensity of the spectral line can then be estimated as

$$I \propto gA\sigma \tag{3.20}$$

This intensity approximation was calculated prior to spectral emission experiments for the various dopant materials discussed in this thesis and played a critical role in spectroscopic examination of experimental results.

Figure 3.6 shows the weighted transition probabilities (gA) for Sn^{8+} - Sn^{13+} calculated by Al-Rabban [40] using the COWAN code suites. The spectral region is between 130-140 angstroms.

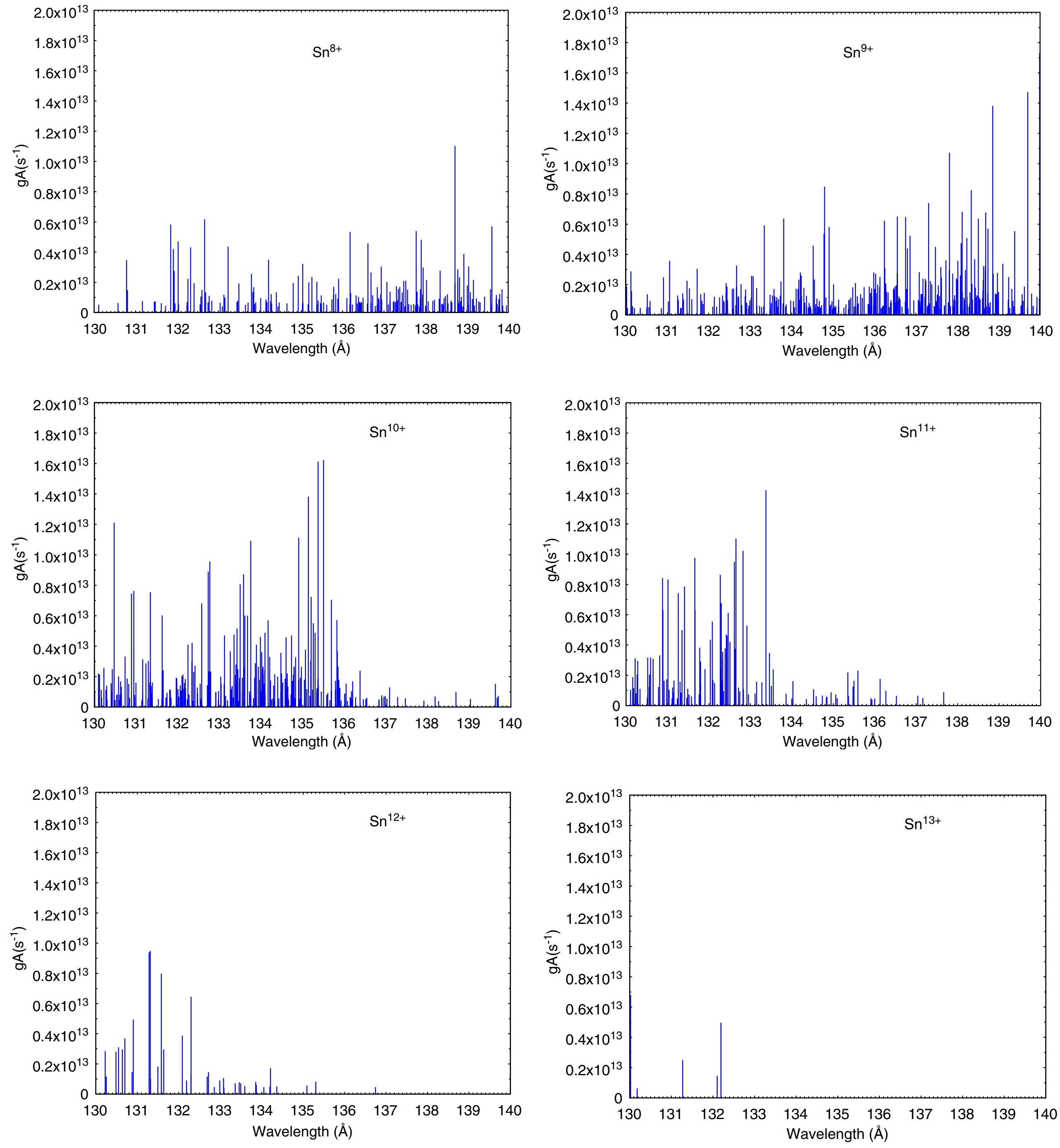

Figure 3.6: Electron temperature and density results at peak of laser input [35]

CHAPTER 4
EXPERIMENTAL CONFIGURATION

The purpose of this thesis is to take the patented, mass-limited doped droplet generation technology [45], developed within LPL and demonstrate its capabilities with various dopant material. LPL has competitively demonstrated much of its efforts in creating a high powered laser produced plasma EUV source using a tin (Sn) doped water droplet. This thesis duplicates previous efforts of the Sn-doped droplets and presents new data on laser plasmas generated from Sn's neighboring elements, Indium (In) and Antimony (Sb).

4.0.3 Droplet Formation

The mass-limited target is a droplet mechanism that derives from jet-dropper systems found in ink jet printers [19]. The concept allows for the formation of droplets of approximately 30 μm in diameter, each containing a small amount of target material mixed with a low-Z material. For the circumstances of this thesis, the low Z material is either deionized water or methanol depending on the target material solubility requirements.

The liquid is forced through an ink-jet capillary, shown in Figure 4.1, and then droplets are formed by applying a vibration of a user defined frequency to break the liquid jet stream as seen in Figure 4.2. This is done by applying a voltage to a piezocrystal that makes contact with the liquid. Droplets are also generated at high repetition rates (10 -100 KHz) which combat satellite generation. The laser beam is externally triggered with a waveform generator such that the laser pulse and droplets are synchronized in phase. This allows for the laser beam to hit droplets centrally, minimizing debris and fully ionizing droplet material [46]. Since the droplet frequencies are much higher than the repetition rate of the laser, unused droplets are captured in a liquid nitrogen cooled receptacle and a motor driven chopper is used to eliminate crystal formation of the droplet material that might occur.

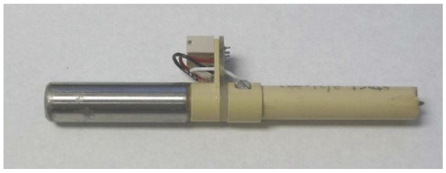

Figure 4.1: Ink jet capillary used for droplet formation

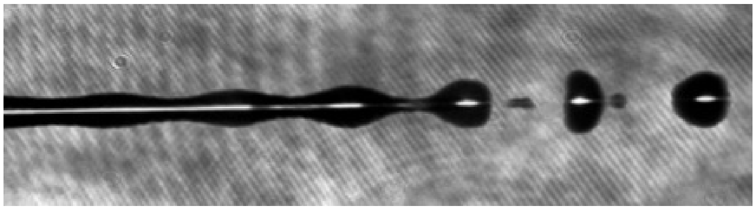

Figure 4.2: Piezo-crystal driven droplet formation

4.0.4 Droplet Dopant Characteristics

The use of Sn to create EUV laser plasmas has a primary application in lithography. Tin's EUV spectral emission around 13.5 nm complements the advancement of Mo/Si multilayer optics as was discussed previously. The mass-limited tin-doped droplets are created by mixing tin chloride ($SnCl_2$), a white crystalline solid compound [47], with deionized water. The molar concentration of tin chloride in the aqueous solution is 4.86 mol/liter. Each droplet contains about 10^{18} Sn atoms.

The molar concentration and hence the amount of dopant per droplet was preserved when preparing both indium and antimony solutions. Indium-doped droplets were created by combining indium chloride ($InCl_3$), a white flakey compound, with deionized water. Indium chloride is highly soluble in water and gives off a small exothermic reaction. Its mixing timing was significantly reduced from that of tin chloride making it easier to prepare. However the solution was thinner then that of its Sn counterpart. This change in viscosity made droplet creation very unstable in air. Under vacuum, it was observed that droplet generation became significantly stable when droplets were generated at a specific frequency of approximately 40 KHz.

Antimony-doped droplets were generated using antimony chloride ($SbCl_3$), a colorless, solid crystal compound. Antimony chloride undergoes hydrolysis with water forming antimony oxy-chloride. The thick viscosity of this solution made it impossible to generate droplets using deionized water. Instead, methanol (CH_3OH) was used as a solvent. The solution also had a significantly shorter mixing time than the tin-doped water droplets and droplets were found to be stable in both air and under vacuum conditions. Table 4.1 shows physical characteristics of the various dopants used to form droplets for this thesis.

Table 4.1: Dopant Characteristics

Atomic Number	**Name**	**Formula**	**Mol. Weight**	**MP** °C	**BP** °C	**Density** $g \cdot cm^{-3}$
49	Indium (III) Chloride	$InCl_3$	221.176	583	–	4.0
50	Tin (II) Chloride	$SnCl_2$	189.615	247.1	623	3.90
51	Antimony (III) Chloride	$SbCl_3$	228.118	73.4	220.3	3.14

4.1 LPL Source Development

The EUV sources discussed throughout this thesis were created in the laser plasma laboratory. The laboratory conditions and facilities are presented in the following subsection.

4.1.1 Vacuum Environment

The vacuum chamber used for the studies presented is 75 cm x 52.5 cm with a depth of 25 cm and a radius of curvature of 72 cm. It has fourteen 7 cm ports separated by an arc length of 8.5 cm which are used to support electrical and mechanical feedthroughs, laser input and various plasma diagnostics. A turbo pump with a 42K RPM rotational speed is attached to the chamber via a 20.32 cm flange. The chamber is capable of pumping down to

10^{-5} Torr, allowing for the transmission of EUV and Soft X-Ray radiation. Target position is determined by the intersection of two low powered 534 nm, green helium-neon laser beams entering the chamber, such that the intersection can be a 90° angle and each of the fourteen ports is equally separated from the target by an angle of 10.5°. With respect to the target, a laser beam enters the chamber at an angle of 42 °. Both a flat-field spectrometer and an EUV energy detector are aligned at angles of 10.5° with respect to the source. A picture of the vacuum chamber is shown in Figure 4.3.

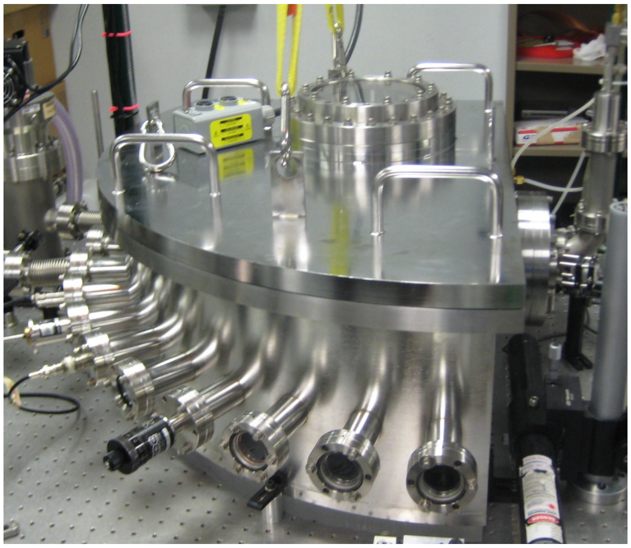

Figure 4.3: Vacuum chamber used for experiments

4.1.2 Solid-State Nd:YAG Laser

The laser used to conduct these experiments is a flash-lamp pumped Nd:YAG system available from Spectra Physics which is operated at a repetition rate of 100 Hz. The laser output wavelength is 1064 nm. The maximum attainable energy is ∼260 mJ with a pulse duration of 9.5 ns. The beam is focused onto the target using an AR coated gradium lens with a 30 mm diameter and an effective focal length of 60 mm. The beam waist was measured to be 26.3 μm using a Spiricon beam profiler after imaging through a 10x microscope objective lens.

4.1.3 Droplet Target Imaging System

The droplets, which are produced at a frequency of approximately 30-40 KHz to maintain stability, are imaged through a single plano-convex lens with an effective focal length of 100 mm. A high powered, 625 nm, red LED generated at the same frequency illuminates the droplets from behind the lens and the magnified image is displayed on a Logitech CCD. Although aberrations are prevalent, the quality of the image is sufficient to observe droplet frequency and stability.

4.1.4 Plasma Diagnostics

4.1.4.1 Flat-Field Spectrometer and Microchannel Plate

Spectral data of the target materials were collected and analyzed on a flat-field spectrometer (FFS) that images wavelengths from 5-20 nm. The configuration of this particular spectrometer is based on the concept of combining a plane diffraction grating with properties of a concave mirror. The spectrometer uses a variably spaced concave grating with a nominal 1200 lines/mm operating at a grazing incidence angle of 3°.

This idea is the basis of the Rowland circle configuration, devised by H.A Rowland, and is a standard for many modern vacuum spectrographs today. The configuration places a concave grating tangentially on a hypothetical circle whose diameter equals that of the radius of curvature of the grating. The traditional configuration of a Rowland circle spectrograph is shown in Figure 4.4. Imaging with a Rowland is accomplished using specialized optics that introduce scattered light into the system, making the set up less sensitive to EUV wavelengths [48].

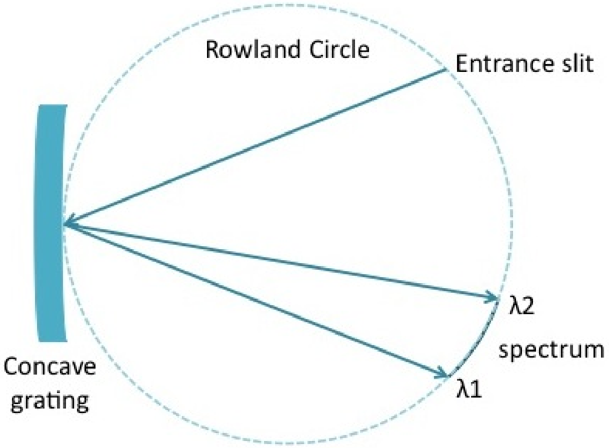

Figure 4.4: Configuration of Rowland circle spectrograph

The main advantage of the FFS is the logical improvement in which the tangential focal curve is removed from the Rowland configuration and is rendered near linear over a spectrum of interest. In this case, the spectrum of interest is 5-20 nm. Resolution is maintained or even improved with a flat field imaging surface and astigmatism is minimized [49, 50, 51]. The configuration of the FFS is shown in Figure 4.5.

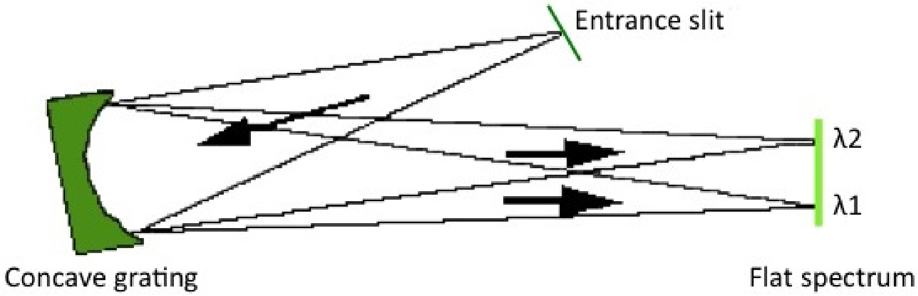

Figure 4.5: Flat field spectrograph configuration

The incidence arm length from the entrance slit to the center of the grating for the particular FFS set up used is 237 mm. The center of the grating to the image plane length is 235 mm [52]. The geometrical arrangement displaying diffraction properties of this particular FFS is shown in Figure 4.6.

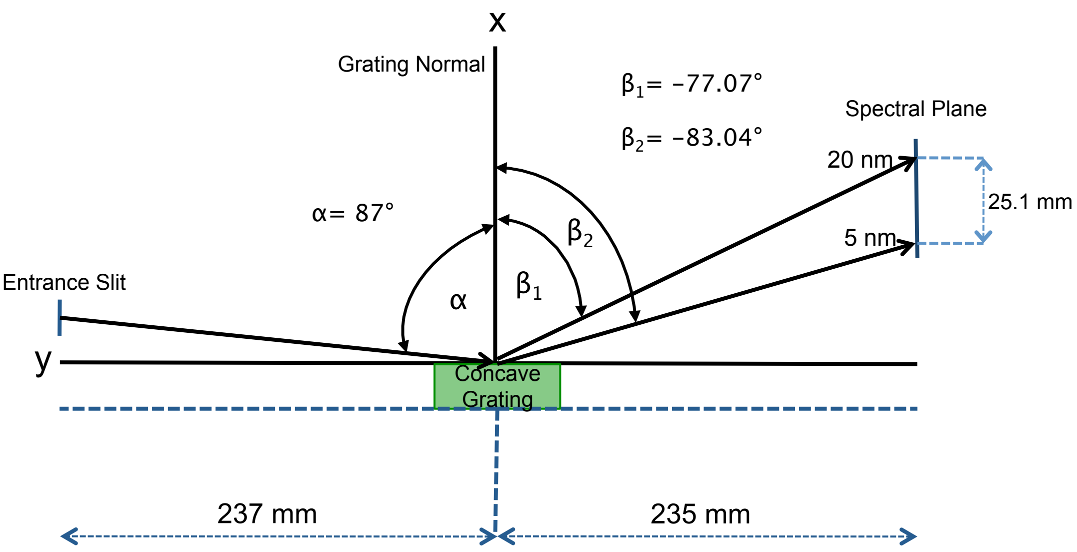

Figure 4.6: Diffraction properties of the flat-field spectrometer

The grating equation,

$$m\lambda = \sigma_0[sin(\alpha) + sin(\beta)] \tag{4.1}$$

where m is the diffraction order, σ_0 is the nominal groove spacing and α and β are the incidence and diffraction angles respectively [49], was used to calculate the first and second order of a green alignment beam. This ensured the calibration of the spectrometer for EUV wavelengths upon the flat detector. Previously, imaging of the first and second order have shown that the grating efficiency for the second order is significantly lower than that of the first order and therefore the second order is not normally detected [53].

The spectral resolution of the FFS, which determines the separation between two spectral peaks that can be detected at the image plane, was measured by Schwanda et al [51].The best resolving power ($\lambda/\Delta\lambda$) was determined to be ≈ 1500 which is between 5-6 nm. The absolute grating efficiency or the amount of incident flux diffracted into the first order normalized to the incident flux on the grating, was also determined. The measurements displayed in Figure 4.7 show that the efficiency is nearly constant between 10-20 nm and decreases almost linearly between the wavelengths of 5-10 nm.

The FFS used in the experiments conducted does not directly image to a charge-coupled device (CCD). Instead, the imaging plane is attached to a micro-channel plate (MCP) as-

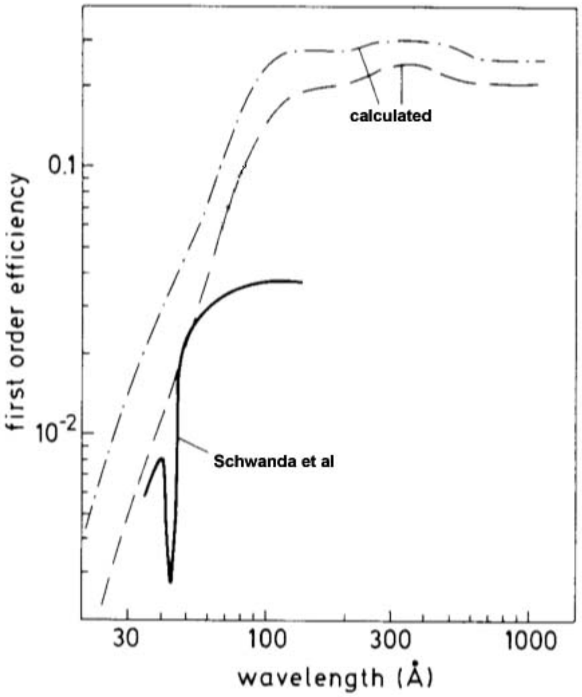

Figure 4.7: First order grating efficiency as a function of wavelength
[51]

sembly which is then coupled to the CCD array. A micro-channel plate is a device used to intensify the photon radiation by multiplication of electrons, similar in function to an electron multiplier. The MCP is configured with two plates, each having 10 μm diameter channels arranged in a chevron (V-like) configuration with a 12 ° pitch [53]. A schematic of the micro-channel plate is shown in Figure 4.8.

An incident ray enters a channel and releases an electron via a photoelectric effect from the wall of the channel. It gains momentum and accelerates across the channel from the potential difference of -1200 V that is applied to the channel. A secondary emission effect takes place where the initial electron strikes the wall of the channel and emits more electrons which in turn continue to hit the channel wall and emit electrons so that at the end of the

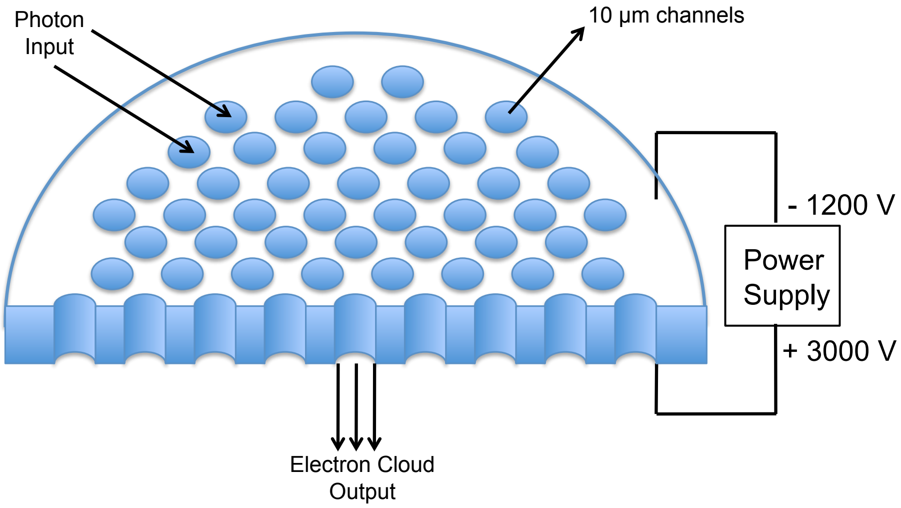

Figure 4.8: Schematic of a micro-channel plate

channel is a cloud of thousands of electrons [54]. The electrons bombard a phosphor screen which is positively biased at 3000 V. Both the positive and negative bias are fixed for the case of these experiments, however, they can be modified to alter the gain. The phosphor screen is fiber-optically coupled to a Photometrics CCD with a square array, 1024 x 1024, with 24 μm pixels. The arrangement of this configuration is shown in Figure 4.9. The spectral resolution of the FFS/MCP imaging configuration is limited by the pixel size of the CCD. The resolution of the image is 0.015 nm/pixel. In view of the fact that the MCP must maintain a pressure of 10^{-7} Torr to function, a differential pumping mechanism in between the vacuum chamber and the FFS has been implemented.

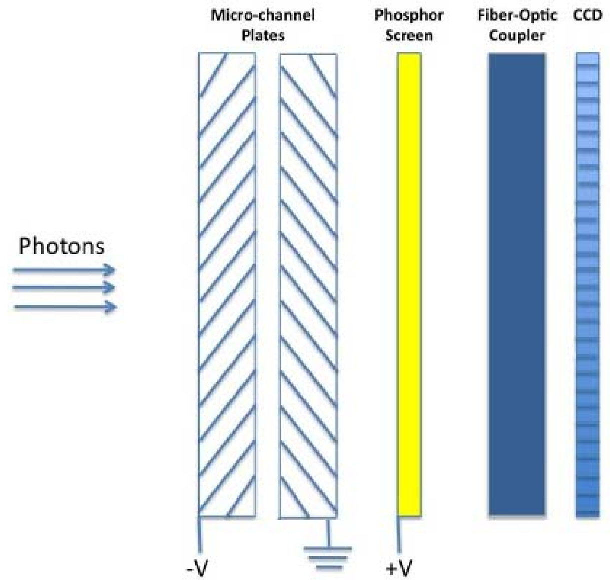

Figure 4.9: MCP Configuration

4.1.4.2 Flying Circus Energy Meter

Although the purpose of this thesis is to perform spectroscopic analysis of mass-limited droplet based laser plasmas, the measurement of EUV energy plays an important role in determining laser to plasma conversion efficiencies. Also coupled to the vacuum chamber is an instrument known in the EUV source development community as the Flying Circus (FC). This instrument, illustrated in Figure 4.10, allows for the measurement of absolute EUV energy at the industry specified 13.5 nm wavelength. Within the FC is a Mo/Si, 25.4 mm, spherical multilayered mirror which is used as a collector and focuses narrow-band EUV radiation from the source onto a photodiode [55].

The photodiode has a spectral responsivity of 0.24 A/W at 13.5 nm with a radiation-hardened entrance window [56]. Between the MLM and the photodiode is a 0.5 μm thick

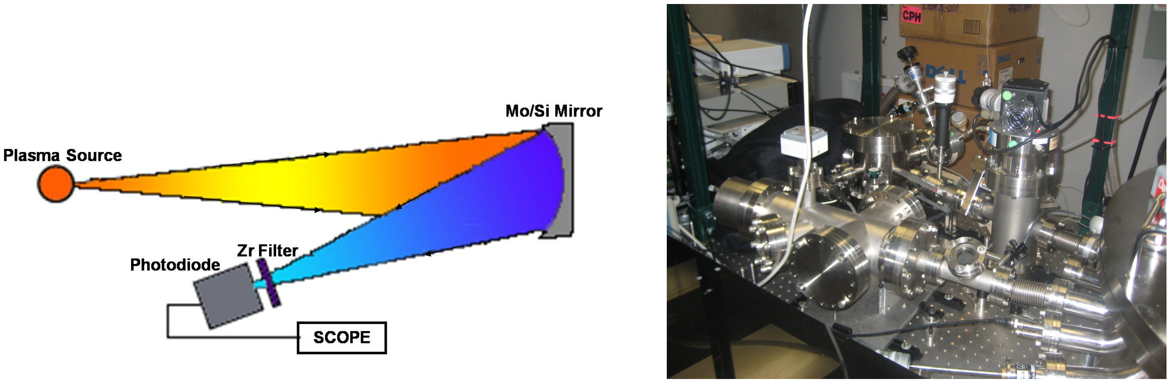

(a) Application of FC (b) FC coupled to chamber

Figure 4.10: Flying Circus Energy Diagnostic

zirconium filter, calibrated by NIST, that is used as a band pass filter for EUV wavelength radiation. The filter's narrowband transmission curve is shown in Figure 4.11

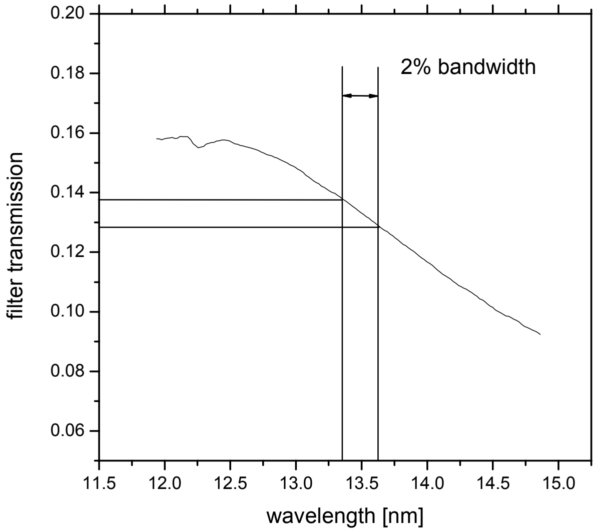

Figure 4.11: Zirconium filter transmission

This EUV energy detector can be cross calibrated with the FFS and used as part of a standard method for estimating conversion efficiency. The Conversion efficiency (CE) for this laser plasma source is a quantitative estimation of how efficiently the laser energy is to converted to EUV radiation. This ratio is calculated to be

$$CE = \frac{E_{BW}}{E_{laser}} \cdot 100\% \tag{4.2}$$

where E_{BW} is the inband EUV energy determined as

$$E_{BW} = K_S \cdot BW_{coeff} \cdot A_{scope} \tag{4.3}$$

In the in-band EUV energy equation, K_S is a constant dependent on the impedance of the oscilloscope, responsivity of the AXUV detector and the collection angle of the EUV source. BW_{coeff} is the bandwidth coefficient whose parameters relate to the spectral emission detected by the FFS and various transmission and reflection properties determined by vacuum conditions and multilayer optics. A_{scope} is the integrated area under the EUV signal waveform as detected by the FC. The in-band EUV energy's linear dependency on the A_{scope} signal makes the flying circus or any energy detector a necessity when determining conversion efficiency requirements for EUVL. This instrumentation was not used for data in this thesis however tin-doped experiments are expected to reflect similar conversion efficiencies ($\approx 2\%$) as was documented in the PhD theses of S. George and C.S Koay [20, 35]. A more detailed breakdown of conversion efficiency has been documented by Schmid et al [57].

CHAPTER 5
EUV SPECTROSCOPY

As mentioned previously, tin-doped laser plasmas have been thoroughly analyzed by the EUV Source Development laboratory at CREOL. This section presents recent experimental results for tin-doped plasmas as well as new spectral data for indium and antimony doped laser plasmas. The chapter begins by examining two techniques for analyzing the various spectra. The first is the use of oxygen lines from methanol and water solvents for pixel to wavelength conversion and the second is the use of COWAN code predictions to identify ion stage transitions within the spectral content. Experimental results and ion stage predictions for each doped plasma then follows.

5.1 Oxygen Lines as a Calibration Tool

Water was one of the first source targets for EUVL because of its strong oxygen O^{5+} (4p-2p) transition that occurs at 13 nm [58]. With the progress of tin and lithium targets, water was dropped as a primary candidate for lithography however, its oxygen lines still play a strong role in quantifying mass-limited targets in the EUV. Since the solvents used for all dopants in this thesis were either deionized water or methanol, oxygen emission was used for the conversion of raw spectral data designated by pixel size, into more feasible wavelength emission.

The online atomic spectra database from NIST [59] lists all known transitions for a majority of the elements and the associated line emission intensities. This data was used to identify wavelengths of the oxygen lines to provide proper pixel to wavelength conversions. Three strong O^{5+} lines located at 13 nm, 15 nm and 17.3 nm were used for most of the calibration in the 5 - 20 nm range that is displayed on the CCD. Figure 5.1 is emission from water and methanol droplets using the flat-field spectrometer. The strong O^{5+} lines that are used for calibration are identified. Other strong O^{5+} lines and O^{4+} lines that are presented in the EUV range are also noted.

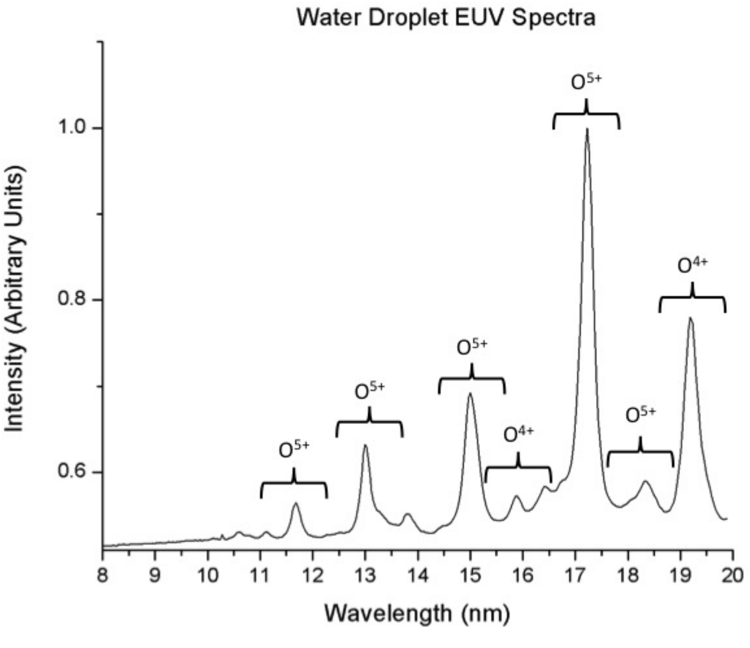

Figure 5.1: Oxygen emission from water and methanol spectra in the EUV

5.2 Identification of ion stages

Prior to experimentation, theoretical weighted oscillator strengths (gf) versus wavelength data was computed for indium, tin and antimony using the COWAN codes by Dr Moza Al-Rabban of Qatar University. Using these computations, the identification of ion stages for the various target compounds is determined. The theoretical spectra is created by convolving the oscillator strength values with a gaussian function of narrow width [11, 34, 35, 60].

The convolution method is simplified by looking at a fabricated collection of oscillator strength values as shown in Figure 5.2. For each wavelength, X_j, an oscillator line strength is represented by Y_j.

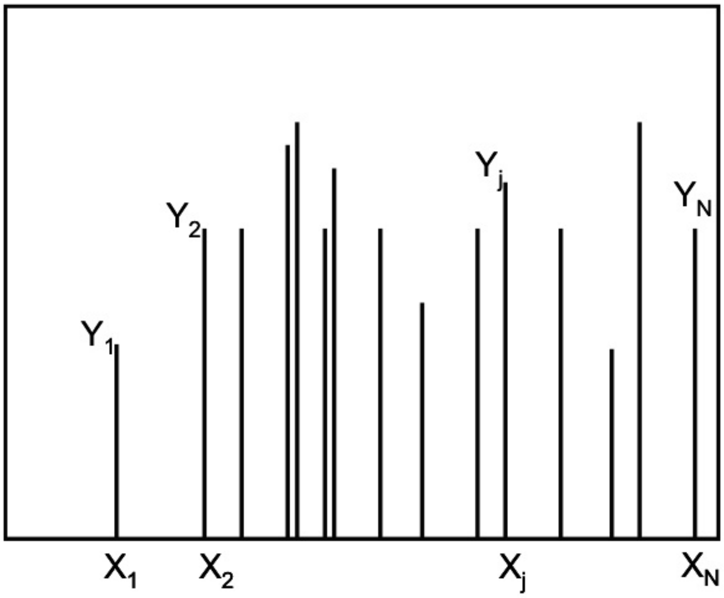

Figure 5.2: A fictitious collection of oscillator strength values (gf)

The simulated spectrum is calculated from Equation 5.1.

$$spec(\lambda) = \sum_{j=1}^{N} Y_j \cdot exp^{\frac{-(\lambda - X_j)^2}{w^2}} \tag{5.1}$$

In the equation, N can be a value in the thousands and w is the width of the Gaussian function. The Gaussian convolution is applied to real data shown in Figure 5.3. The convolved data is presented in Figure 5.4 [35]. The number of lines, N, is approximately 50. The small number of lines and the large separation show the convolution process quite clearly. The COWAN calculations used for the identification of ion stages has a larger number of lines that often crowd among themselves. The Gaussian features are normally not as intelligible as is demonstrated in Figure 5.4.

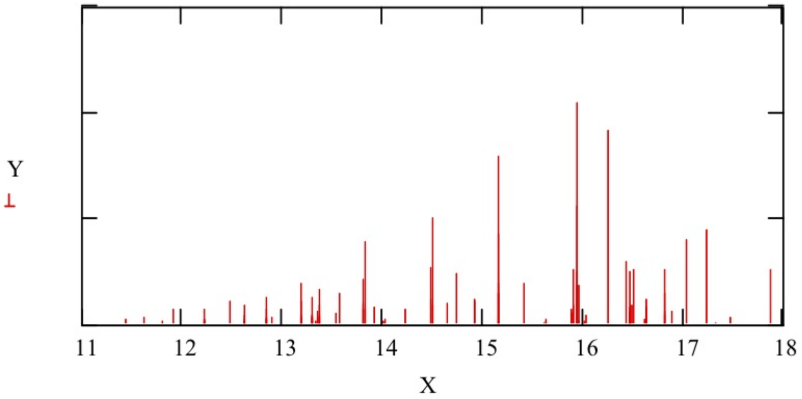

Figure 5.3: An example of oscillator strength data from the COWAN codes where N = 50 and the x-axis is wavelength in nanometers

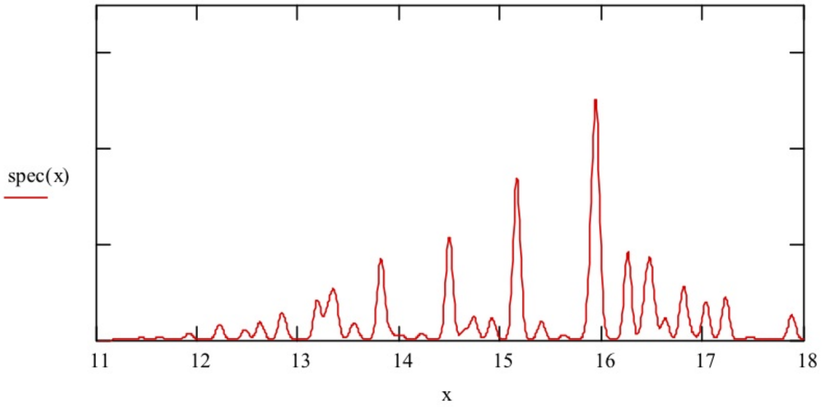

Figure 5.4: Gaussian convolution of data from Figure 5.3 using Equation 5.1

The subsequent sections present results from the various laser plasma targets as well as the identification of the ion stages using this method.

5.3 Spectral Analysis of Tin-doped Laser Plasma

Figure 5.5 is spectra from a tin-doped laser plasma with a laser intensity of $5 \times 10^{11}\ W/cm^2$. The peak of the Sn UTA is at 13.5 nm. As have been shown in previous studies, plasma temperatures are expected to be in the range of 30 - 45 eV at 13.5 nm and electron densities approximate the critical density (10^{21}cm^{-3}) [11, 20, 35] .

Figure 5.6 is synthetic tin emission spectra created by taking COWAN code predictions of oscillator strengths of all the transitions for each of the S^{+7} to Sn^{+12} ions in the 13 nm vicinity and performing the discrete numerical convolution method described previously for a Gaussian function with w= 0.05. In the theoretical spectra shown, the region of intense emission for tin shifts towards shorter wavelengths as the ionization increases. It has been

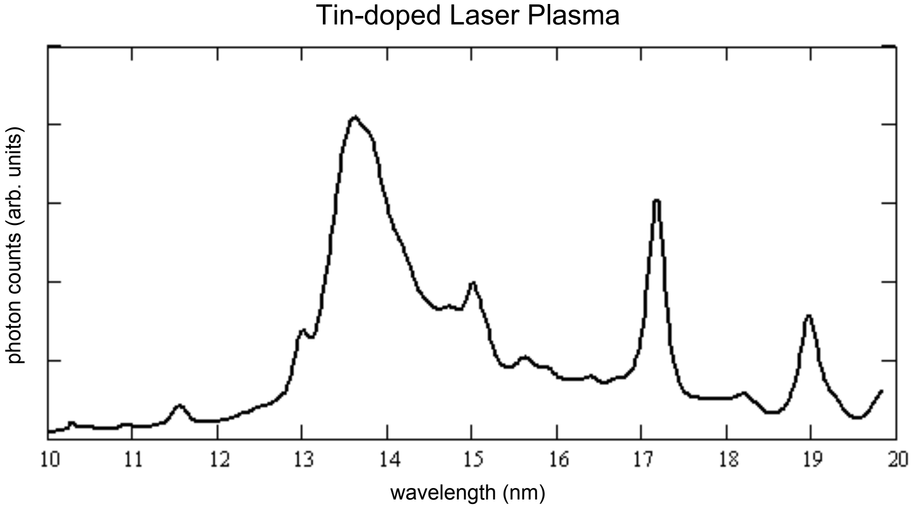

Figure 5.5: Spectra from a mass limited tin-doped laser plasma with a laser intensity of 5×10^{11} W/cm^2

proven in previous works at LPL that as laser intensity is increased, higher ionizations dominate [11, 20, 35]. This also appears to be the case in the real spectrum for a tin-doped laser plasma shown in Figure 5.5. Comparing this result to the theoretical spectra, it is clear to see that transitions Sn^{+9} to Sn^{+11} highly influence the spectra for the laser intensity of 5×10^{11} W/cm^2.

Using simple ionization modeling, the optimal plasma temperature for the creation of tin ions in the 13.5 nm vicinity has been predicted. The calculated fractional ion concentration in a Sn plasma as a function of electron temperature for an electron density of 10^{21} cm^{-3} is shown in Figure 5.7 [34, 40, 61, 62]. The prediction shows that optimum production of 13.5 nm UTA occurs at an electron temperature of 30 eV where the Sn^{+9} - Sn^{+11} transitions dominate.

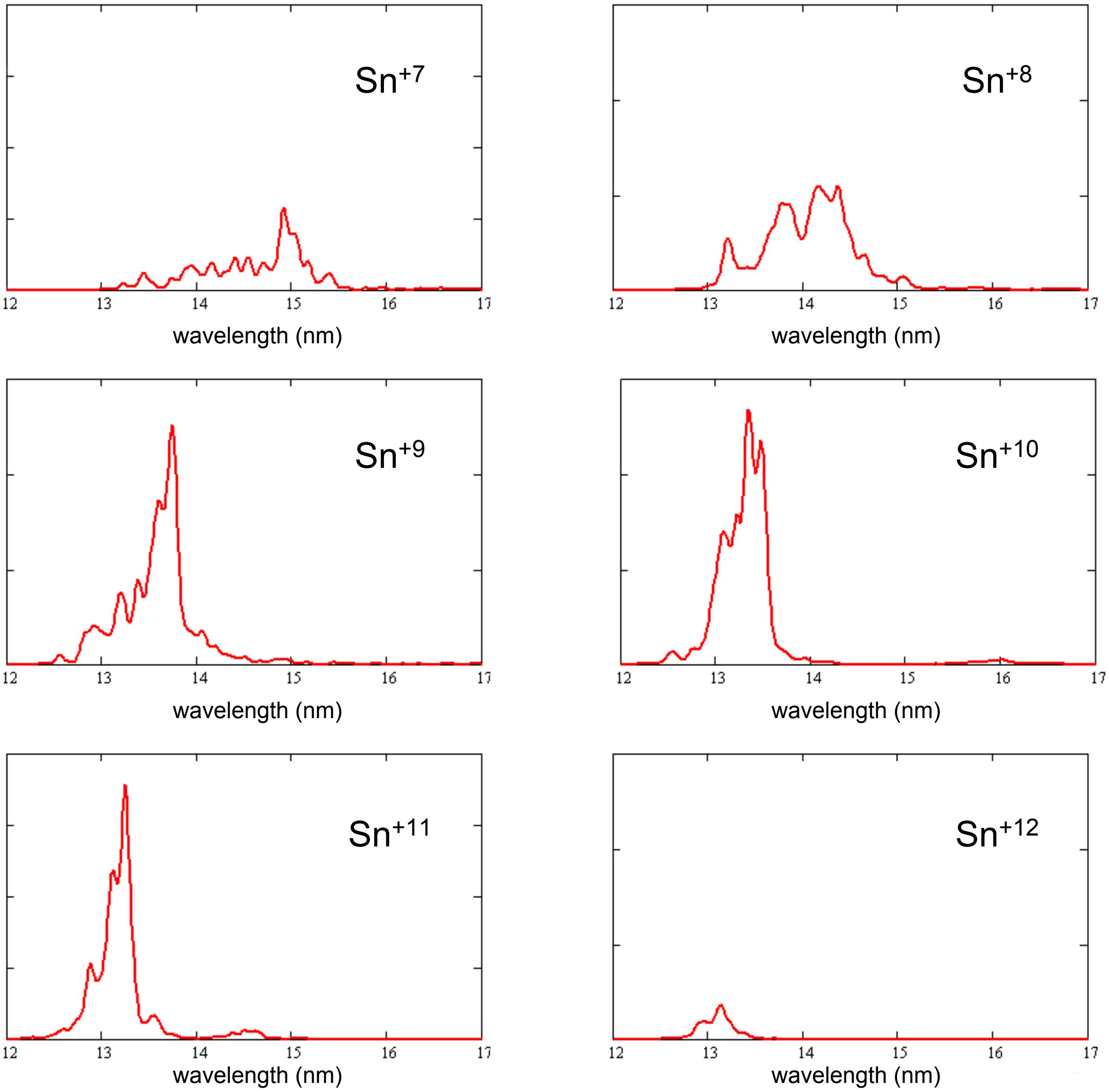

Figure 5.6: Synthetic spectra from COWAN code predictions of oscillator strengths for all Sn transitions in the 13 nm region

5.4 Spectral Analysis of Indium-doped Laser Plasma

Although indium and antimony have different chemical properties than that of tin, the law of periodicity arranges them as neighbors on the periodic table. H.G Moseley's realization that

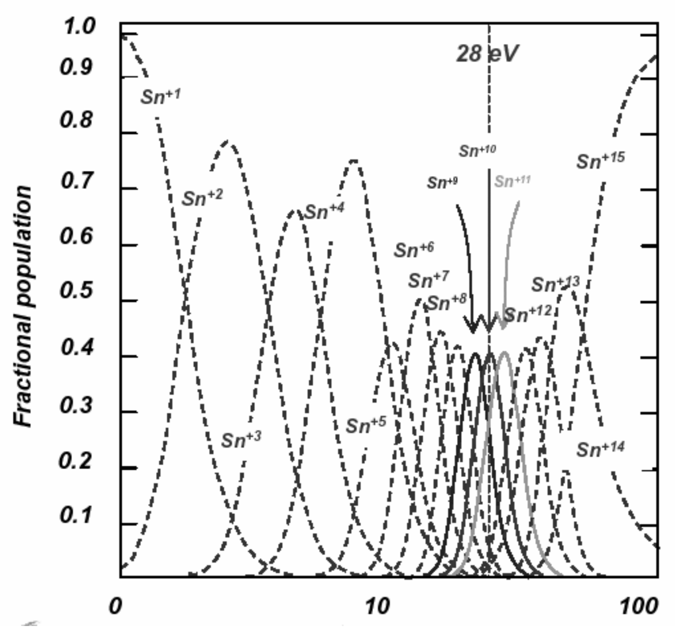

Figure 5.7: Calculated fractional ion population in a Sn plasma as a function of plasma temperature for an electron density of $10^{21}\mathrm{cm}^{-3}$

the wavelength of X-Rays emitted by a given element is relative to that element's atomic number [63] is verified by looking at the EUV spectral emission of mass-limited indium and antimony laser plasmas.

Figure 5.8 shows the spectral emission from an indium doped laser plasma. The emission peaks at 14.5 nm. By looking at the COWAN code predictions for indium ascribed to a Gaussian function with $w = 0.05$ as displayed in Figure 5.9 , it can be reasoned that the ionic transitions of In^{+8} - In^{+10} dominate in the EUV.

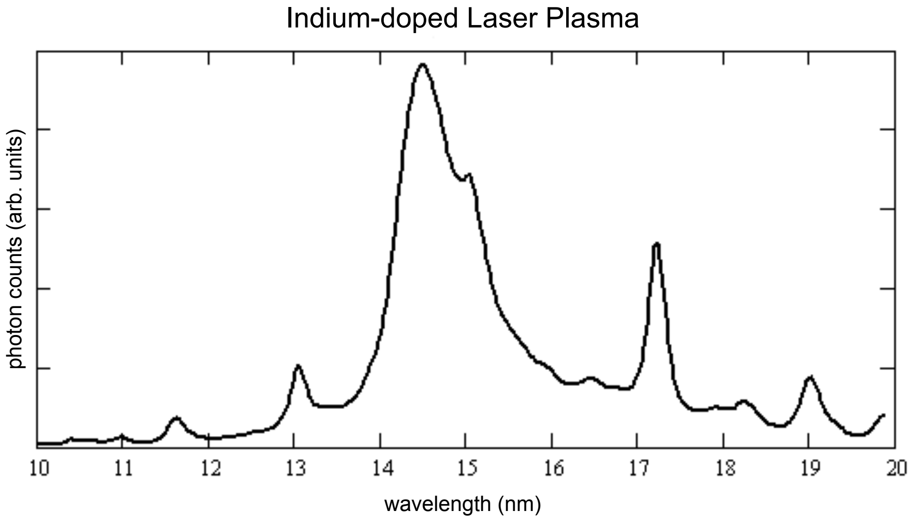

Figure 5.8: Spectra from a mass limited indium-doped laser plasma with a laser intensity of $5 \times 10^{11}\ W/cm^2$

5.5 Spectral Analysis of Antimony-doped Laser Plasma

Figure 5.10 is spectral emission from an antimony doped methanol droplet target. The radiation in the EUV for antimony peaks at approximately 12.8 nm for the laser input of $5 \times 10^{11}\ W/cm^2$. Since the in-band energy extends ±1 nm from the peak radiation, the O^{5+} oxygen line used for wavelength to pixel conversion of previous plasmas at 13 nm is impractical. Instead, antimony was calibrated using the 15 nm and 17.2 nm O^{5+} lines as well as an O^{4+} spectral line existing at 19.3 nm shown in Figure 5.1

Synthetic spectra from the COWAN code predictions for antimony is displayed in Figure 5.11. The data was ascribed to the same Gaussian function as Sn and In spectra with w= 0.05. Emission around the peak at 12.8 nm is assumed to be from Sb^{10+} - Sb^{12+}.

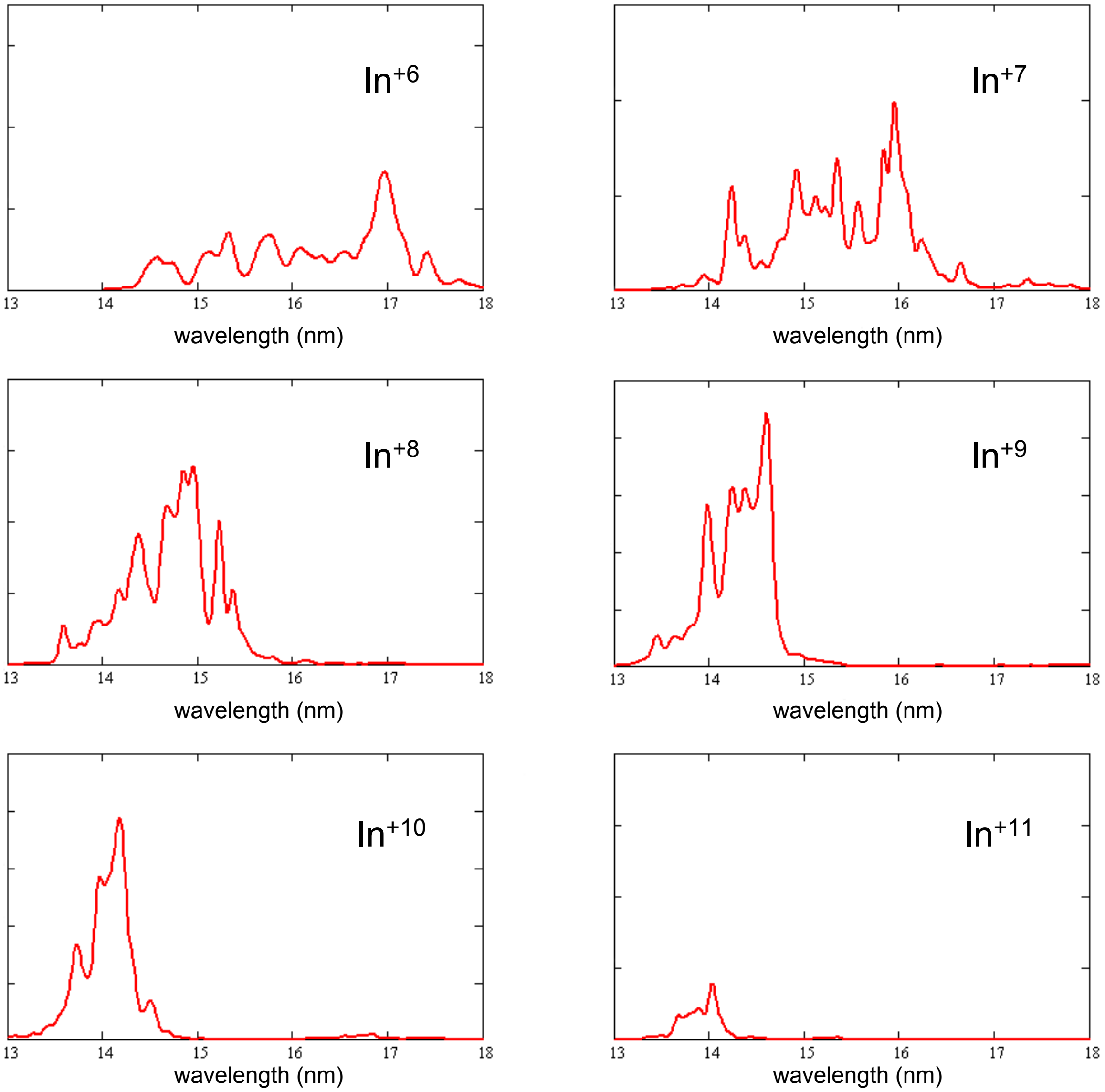

Figure 5.9: Synthetic spectra from COWAN code predictions of oscillator strengths for all In transitions in the 13 nm region

Since indium, tin and antimony exist as periodic neighbors, the ionization transitions for maximum emission in the EUV for the same given laser input is expected to have the same electron configuration. This is proven by the synthetic spectra developed from the COWAN

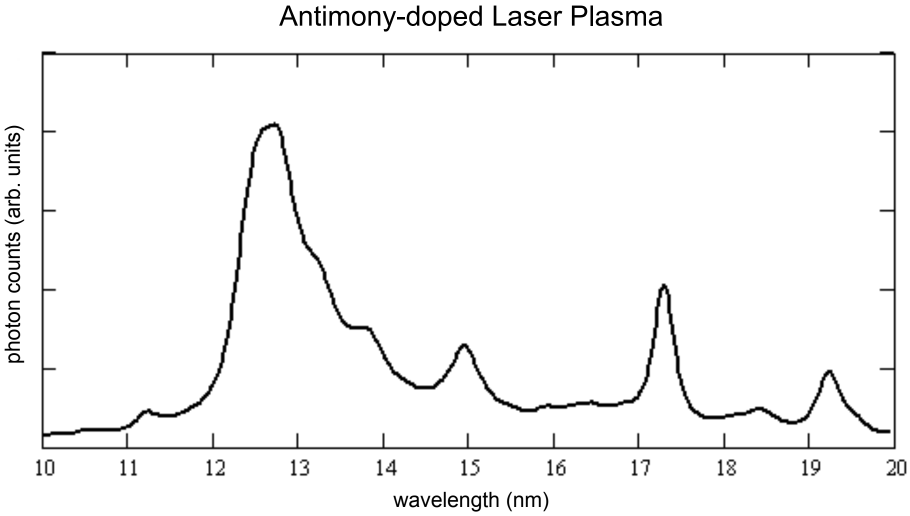

Figure 5.10: Spectra from a mass limited antimony-doped laser plasma with a laser intensity of 5×10^{11} W/cm^2

suites for each of the plasmas created and is demonstrated from the experimental results. Peak emission for indium, tin and antimony initializes at In^{8+}, Sn^{9+} and Sb^{10+} respectively. These transitions all share the electron configuration [Kr] $4d^5$.

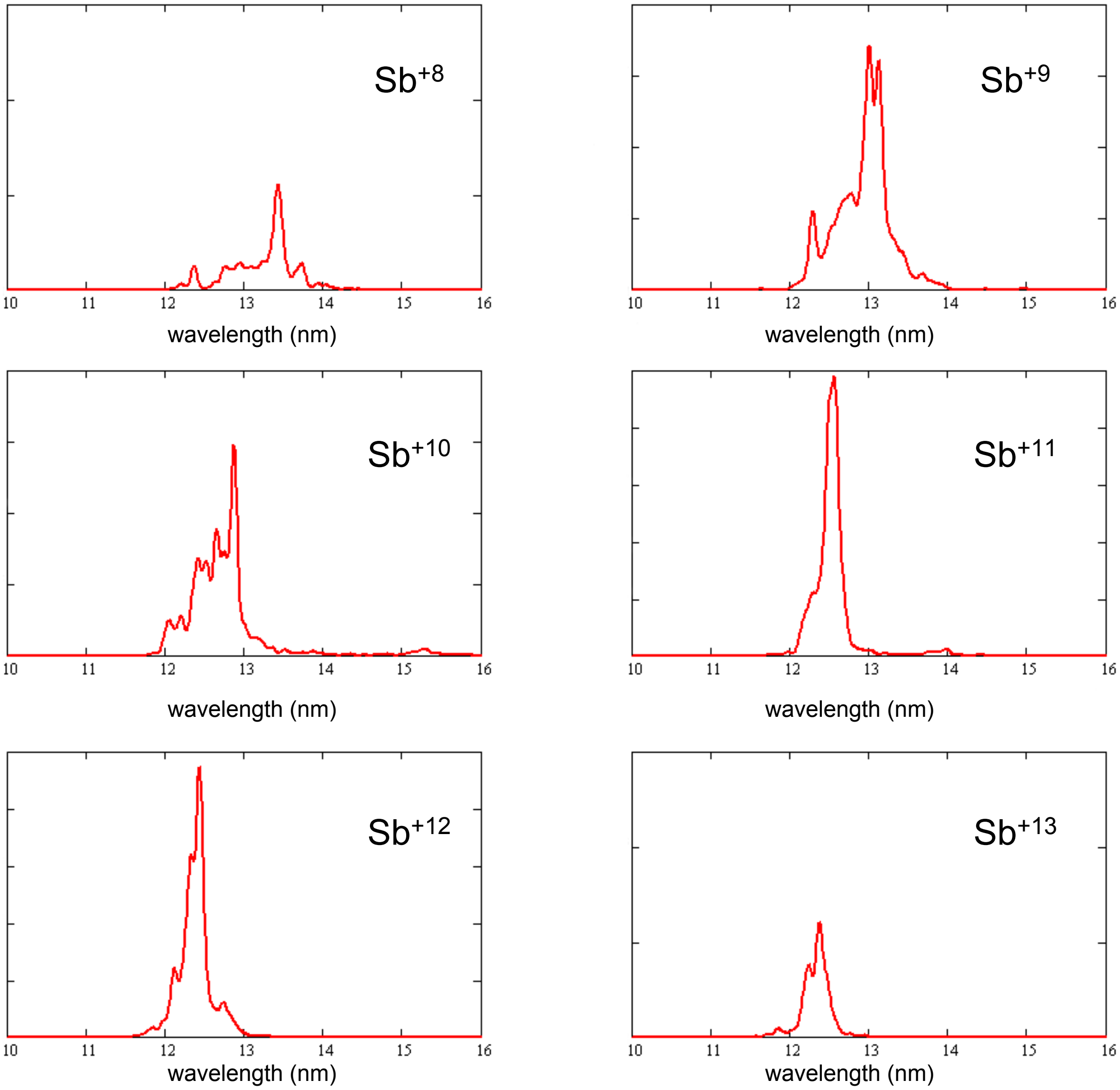

Figure 5.11: Synthetic spectra from COWAN code predictions of oscillator strengths for all Sb transitions in the 13 nm region

CHAPTER 6
SUMMARY AND FUTURE WORK

The Laser Plasma Laboratory within the Townes Laser Institute at CREOL has presented extensive work on the mass-limited droplet based laser plasma. The target's feasibility as a source for EUV lithography is established by its ability to attain high repetition rates as well as its flexibility in accommodating various laser and target architectures. The concept of fully ionizing droplets also appeases debris concerns within the EUV source development community.

The work presented in this document duplicates previous efforts of creating laser plasmas from a tin-doped water droplet. New laser plasma results from indium and antimony doped droplets is also presented. Using a flat-field spectrometer as a plasma diagnostic, spectral emission in the EUV for each of the droplet based plasmas were captured and quantified. COWAN code oscillator strength predictions for all of the dopant material were convolved with a Gaussian function to create synthetic spectra. Comparing experimental findings for the dopant materials with their respective theoretical spectrum allowed for the identification of ion stages that resulted in maximum EUV emission.

The versatility of the mass-limited source concept will continue to be a prolonged study for various dopant material within LPL. Indium and Antimony plasmas have demonstrated favorable characteristics for sources of Extreme Ultraviolet radiation. Vorpal, the hybrid plasma and beam simulation code will be integrated into the studies of these plasmas, to optimize emission in the EUV and Soft X-Ray.

Although the EUV Source development community has made continuous success in the adaptation of a plasma source for EUVL, there are still many source requirements that are yet to be met. Future work in the EUV source development lab at LPL will also involve a continued effort on creating a mass-limited laser plasma source through experimentation with various laser and target configurations.

APPENDIX A

Figure 2.2 is courtesy of the Australian Synchrotron Facility Website. Please see below for granted permission statement.

Dear Reuvani

Do you mean the bending magnet, wiggler and undulator pictures from the following webpage? http://www.synchrotron.org.au/index.php/synchrotron-science/about-synchrotrons/how-is-synchrotron-light-created

If these are the pictures you mean, you have permission to use them in your masters thesis, but not for any other purpose.

Please acknowledge that the diagrams are courtesy of the Australian Synchrotron.

Thank you for your interest in the Australian Synchrotron.

Best wishes

Nancy Mills

Nancy Mills — Publications Coordinator — Australian Synchrotron p: (03) 8540 4155 — f: (03) 8540 4200 — m: 0408 336 434 nancy.mills@synchrotron.org.au — www.synchrotron.org.au 800 Blackburn Road, Clayton, Victoria 3168

From: info Sent: Saturday, 23 January 2010 9:47 AM To: info Subject: Contact from website

Hello,

You have received a comment from AS website with information below:

First name: Reuvani

Email Address: reuvani@creol.ucf.edu

Message: Hi, I would like to know if I can have permission to use some of the pictures from the synchrotron science portion of your website to put in a small section of my master's thesis. I am studying laser plasma EUV sources and I would like to use the pictures on different bending mechanisms for the booster ring portion of the synchrotron to identify other methods of euv radiation

LIST OF REFERENCES

[1] D. Attwood, *Soft X-Rays and Extreme Ultraviolet Radiation.* Cambridge University Press, 1999.

[2] C. Phipps, *Laser Ablation and its Applications.* Springer Science + Business Media, 2007.

[3] J. Underwood and J. T.W. Barbee, "Layered synthetic microstructures as Bragg diffractors for X rays and extreme ultraviolet: theory and predicted performance," *Applied Optics*, vol. 20, pp. 3027–3034, 1981.

[4] E. Spiller, Ed., *Soft X-Ray optics.* SPIE Press, 1994.

[5] W. Soer, P. Gawlitza, and et al, "Extreme Ultraviolet multilayer mirror with near-zero IR reflectance," *Optics Letters*, vol. 34, p. 3680, December 2009.

[6] C. Montcalm, S. Bajt, P. Mirkarimi, and et al, "Multilayer reflective coatings for extreme-ultraviolet lithography," in *Emerging Lithographic Technologies II*, vol. 3331. SPIE Press, 1998.

[7] S. Bajt, J. B. Alameda, and et al, "Improved reflectance and stability of mo-si multilayers," *Optical Engineering*, vol. 41, p. 1797, August 2002.

[8] E. Gullikson, "Multilayer reflectivity," Center for X-Ray Optics, Tech. Rep., 2007.

[9] S. Yulin, N. Benoit, and et al, "Interface-engineered EUV multilayer mirrors," *Microelectronic Engineering*, vol. 83, pp. 692–694, 2006.

[10] I. T. R. for Semiconductors, "ITRS lithography roadmap for semiconductors," Tech. Rep., 2007. [Online]. Available: http://www.itrs.net/links/2007itrs/2007_chapters/2007_Lithography.pdf

[11] M. Richardson, *Extreme Ultraviolet Lithography.* McGraw-Hill Companies, 2009, ch. 3.

[12] O. Wood, C.-S. Koay, K. Petrillo, and et al, "Integration of EUV lithography in the fabrication of 22-nm node devices," in *Alternative Lithographic Technologies*, vol. 7271. SPIE Press, 2009.

[13] K. Ota, Y. Watanabe, V. Banine, and H. Franken, *EUV Sources for Lithography.* SPIE Press, 2005, ch. 2.

[14] H. Meiling, N. Buzing, K. Cummings, and et al, “EUVL System: Moving Towards Production,” in *Alternative Lithographic Technologies*, vol. 7271. SPIE Press, 2009.

[15] E. Hendrickx, A. Goethals, and et al, “Full field EUV Lithography: Lessons learnt on EUV ADT imaging, EUV resist, and EUV reticles,” in *Lithography Asia 2008*, vol. 7140. SPIE Press, 2008.

[16] J. Hermans, B. Baudemprez, G. Lorusso, and et al, “Stability and imaging of the EUV Alpha Demo Tool,” in *Alternative Lithographic Technologies*, vol. 7271. SPIE Press, 2009.

[17] J. Harvey, W. Zmek, and C. Ftacias, “Interface-engineered EUV multilayer mirrors,” *Microelectronic Engineering*, vol. 83, pp. 692–694, 2006.

[18] L. Juschkin and R. Freiberger, “Two magnification steps EUV microscopy with a Schwarzchild objective and an adapted zone plate lens,” in *EUV and X-Ray Optics: Synergy between Laboratory and Space*, vol. 7360. SPIE Press, 2009.

[19] C. Keyser, “Optical and spectral characterization of the water droplet laser plasma EUV source,” PhD, University of Central Florida, 2003.

[20] S. A. George, “Spectroscopic studies of laser plasmas for EUV sources,” PhD, University of Central Florida, 2007.

[21] Berkeley Laboratory, “The Advanced Light Source,” December 2009. [Online]. Available: http://www.als.lbl.gov

[22] A. S. Company, “Synchrotron science,” Tech. Rep., 2008. [Online]. Available: http://www.synchrotron.org.au/content.asp?Document_ID=97

[23] K. Suzuki and B. W. Smith, *Microlithography: science and technology.* CRC Press, 2007.

[24] K. Takenoshita, “Debris characterization and mitigation of droplet laser plasma sources for EUV lithography,” PhD, University of Central Florida, 2006.

[25] U. Stamm, G. Schriever, and J. Kleinschmidt, *EUV Sources for Lithography.* SPIE Press, 2005, ch. 14.

[26] L. Shmaenok, C. Bruijn, H. Fledderus, and et al, “Demonstration of a foil trap technique to eliminate laser plasma atomic debris and small particulates,” in *Emerging Lithographic Technologies II*, vol. 3331. SPIE Press, 1998.

[27] J. Rocca, M. Murnane, and D. Attwood, “EUV ERC Annual Report Volume II,” Engineering Research Center for Extreme Ultraviolet Science and Technology, Tech. Rep., 2009.

[28] M. Richardson, *EUV Sources for Lithography.* SPIE Press, 2005, ch. 26.

[29] W. L. Kruer, *The Physics of Laser Plasma Interactions.* Westview Press, 2003.

[30] S. E. Grantham, “High powered, short-pulsed laser faculity for hard x-ray and hot electron generation,” PhD, University of Central Florida, 1999.

[31] D. Giulietti and L. Gizzi, “X-ray emission from laser-produced plasmas,” *La Rivista del Nuovo Cimento*, vol. 21, p. 10, 1998.

[32] B. Handy, L. Acton, and et al, “The transition region and coronal explorer,” *Solar Physics*, vol. 187, p. 229, 2002.

[33] C. Keyser, G. Schriever, and M. Richardson, “Studies of high-repetition-rate laser plasma EUV sources from droplet targets,” *Applied Physics A: Materials Science and Processing*, vol. 77, pp. 217–221, 2003.

[34] M. Al-Rabban, M. Richardson, and et al, *EUV Sources for Lithography.* SPIE Press, 2005, ch. 10.

[35] C.-S. Koay, “Radiation studies of the tin-doped microscopic droplet laser plasma light source specific to EUV lithography,” PhD, University of Central Florida, 2006.

[36] H. Baldis, E. Campbell, and W. Kruer, *Physics of Laser Plasma.* North-Holland Publishing, 1991.

[37] W. Lochte-Holtgreven, *Plasma Diagnostics.* North-Holland Publishing, 1995.

[38] Y. B. Zel’dovich and Y. P. Raizer, *Physics of Shock Waves and High-Temperature Hydrodynamic Phenomena.* Dover Publications, 1966.

[39] D. Salzmann, *Atomic Physics in Hot Plasmas.* Oxford University Press, 1998.

[40] M. Al-Rabban, “Term structure of 4d-electron configurations and calculated spectrum in Sn-isonuclear sequence,” *Journal of Quantitative Spectroscopy and Radiative Transfer*, vol. 97, p. 278, 2006.

[41] J. Christiansen, D. Ashby, and K. Roberts, “MEDUSA: a one-dimensional laser fusion code,” *Computer Physics Communication*, vol. 7, pp. 271–287, 1974.

[42] Tech-X Corporation, “VORPAL User Guide,” December 2009. [Online]. Available: http://www.txcorp.com/pdf/VORPAL/documentation/VORPAL-4.0.0_User_Guide.pdf

[43] R. D. Cowan, *The Theory of Atomic Structure and Spectra.* University of California Press, 1981.

[44] O. Svelto, *Principles of Lasers.* Plenum Press, 1998.

[45] M. Richardson, “EUV, XUV and X-Ray wavelength sources created from laser plasma produced from liquid metal solutions,” U.S. Patent 11 503 703, 2006.

[46] C.-S. Koay, K. Takenoshita, E. Fujiwara, and et al, “Spectroscopic studies of the Sn-based droplet laser plasma EUV source,” in *Emerging Lithographic Technologies VIII*, vol. 5374. SPIE Press, 2004.

[47] D. R. Lide, Ed., *Handbook of Chemistry and Physics: 82nd Edition.* CRC Press, 2001.

[48] D. Cotton, T. Cook, and S. Chakrabarti, “Single-element imaging spectrograph (SEIS) for magnetospheric imaging,” in *Ultraviolet Instrumentation for Magnetospheric Imagery I*, vol. 2008. SPIE Press, 1993.

[49] T. Kita, T. Harada, and et al, “Mechanically ruled aberration corrected concave gratings for a flat-field grazing incidence spectrograph,” *Applied Optics*, vol. 25, p. 4228, 1986.

[50] C. Palmer, *Diffraction Grating Handbook.* Newport Corporation, 2005.

[51] W. Schwanda, K. Eidmann, and M. Richardson, “Characterization of a flat-field grazing incidence XUV spectrometer,” *Journal of X-Ray Science and Technology*, vol. 4, pp. 8–17, 1993.

[52] M. Richardson, C.-S. Koay, K. Takenoshita, and et al, “Diagnostics for laser plasma EUV sources,” in *26_{th} International Congress on High Speed Photography and Photonics*, vol. 5580. SPIE Press, 2005.

[53] M. A. Klosner, “Intense capillary discharge plasma extreme-ultraviolet sources for EUV lithography and other EUV imaging applications,” PhD, University of Central Florida, 1998.

[54] M. V. Zombeck, “Microchannel plate principles of operation,” Harvard Smithsonian Astrophysical Laboratory, Tech. Rep., 2003.

[55] M. Richardson, C.-S. Koay, K. Takenoshita, and et al, “High conversion efficiency mass-limited Sn -based laser plasma source for extreme ultraviolet lithography,” *Journal of Vacuum Science and Technology B: Microelectronics and Nanometer Structures*, vol. 22, p. 785, 2004.

[56] International Radiation Detectors, Inc., “AXUV Photodiodes Report and Operation Principles,” 1991. [Online]. Available: http://www.ird-inc.com/axuvope.html

[57] T. Schmid, S. George, J. Cunado, and et al, “High repetition-rate LPP-source facility for EUVL,” in *Emerging Lithographic Technologies XI*, vol. 6517. SPIE Press, 2007.

[58] F. Jin, M. Richardson, G. Shimkaveg, and D. Torres, “Characterization of a laser plasma water droplet EUV source,” in *Proceedings of SPIE*, vol. 2523. SPIE Press, 1995.

[59] National Institutes of Standard and Technology, "NIST Atomic Spectra Database," December 2009. [Online]. Available: http://physics.nist.gov/PhysRefData/ASD/index.html

[60] J. White, P. Hayden, and et al, "Simplified modeling of 13.5 nm unresolved transition array emission of a Sn plasma and comparison with experiment," *Journal of Applied Physics*, vol. 98, 2005.

[61] C. Koay, S. George, K. Takenoshita, and et al, "High conversion efficiency microscopic tin-doped droplet target laser-plasma source for EUVL," vol. 5751. SPIE Press, 2005.

[62] M. Richardson, C.-S. Koay, K. Takenoshita, and et al, "Laser plasma EUVL sources: progress and challenges," in *Emerging Lithographic Technologies VIII*, vol. 5374. SPIE Press, 2004.

[63] J. Heilbron, "The Work of H.G.J. Moseley," *ISIS*, vol. 57, pp. 336–364, 1966.